Numerical study of the stress singularity in stick-slip flow of the Phan-Thien Tanner and Giesekus fluids

J.D. Evans*
Department of Mathematical Sciences, University of Bath,
Bath, BA2 7AY, United Kingdom

J.A. Cuminato, I.L. Palhares Junior†
Departamento de Matemática Aplicada e Estatística
Instituto de Ciências Matemática e Computação, Universidade de São Paulo,
13566-590 São Carlos, SP, Brazil

C.M. Oishi‡
Departamento de Matemática e Computação, Faculdade de Ciências e Tecnologia,
Universidade Estadual Paulista "Júlio de Mesquita Filho"
19060-900 Presidente Prudente, SP, Brazil

July 4, 2019

Abstract

Stick-slip flow is a challenging viscoelastic benchmark problem due to the presence of a separation or transition point at the die exit where a sudden change in flow boundary conditions occur. We present numerical simulations of transient planar stick-slip flow of the Phan-Thien–Tanner (PTT) and Giesekus fluids, investigating the polymer stress behaviour around the stress singularity at the stick-slip point, confirming the asymptotic results presented in Evans et al., Physics of Fluids, **29**, 1–33, 2017. In order to improve the numerical knowledge about this viscoelastic benchmark problem, two distinct mathematical methodologies are used for comparison in the computational simulations: the Cartesian and the natural stress formulations. The former, is widely applied in computational rheology, whilst the latter is used for the first time in the context of this problem. The natural stress formulation gives improved convergence results both temporally and spatially near the singularity, whilst maintaining the same global flow characteristics as the Cartesian.

Keywords: Numerical study, viscoelastic fluids, Cartesian stress formulation, natural stress formulation, singularity, boundary layer, stick-slip problem

* e-mail: masjde@bath.ac.uk
† e-mail: irineulopespalhares@gmail.com, Phone: +55 18 981793481
‡ e-mail: cassio.oishi@unesp.br, Phone: +55 18 32295623

1 Introduction

A common industrial processing situation involves the extrusion of molten polymers through a die. The dies tend to be rectangular (slit) or capillary (cylindrical) and the polymer is usually melted and pumped through fixed channels and orifices to provide a steady stream of a given cross-sectional profile [1]. It is a process that has received much experimental and theoretical attention due to the following features:

1. Die swell: on leaving the channel, the extrudate can expand (i.e swell) significantly when viscoelastic materials are involved instead of Newtonian [2];

2. Stress singularity: on leaving the die there is an abrupt change in boundary conditions from one involving velocity on the die wall to that of a stress free surface condition outside the die [2–7];

3. Extrudate distortions and fracture: various morphological distortions in the extrudate surface can occur when the wall shear stress exceeds critical values. The surface can change from being smooth to exhibiting sharkskin, spurt (sometimes referred to as stick-slip in reference to changing no-slip and slip wall velocity conditions) and fracture. These instabilities have attracted a lot of attention, see for example, Petrie & Denn [8], Denn [9, 10], Larson [11], Graham [12], and more recently, Kwon [13].

Our focus here is on the situation in which the extrudate's free surface remains smooth and does not deform. This is a particular case of die swell, which is also often referred to as stick-slip flow (in reference to the change of boundary conditions inside the die to outside). It allows investigation of the singular stress behaviour at the die exit, before proceeding to more complex and involved situations. Stick-slip is one of five benchmark problems [14] proposed for the testing and comparison of numerical techniques.

Real polymeric fluids exhibit properties in simple shear flows such as shear thinning and non-zero normal stress differences [2, 15]. Models such as PTT [16, 17] and Giesekus [18], capture such effects well and correct deficiencies of simpler models, such as Oldroyd-B [2, 19], which possesses inifinite stresses at finite elongational rates. This is particularly relevant for stick-slip, as elongational flow dominates after emergence of the polymeric fluid from the die. It is also worth remarking that the PTT and Giesekus models are not only applicable to polymer processing of plastics, elastomers, suspensions and certain food products [20], but also to other problems in Rheology, such as non-Newtonian haemodynamics [21, 22], the extrusion process [23, 24], double-layer optical fibers [25], fluid damper problems [26] and microfluidic flows [27, 28], to name only a few.

In previous work [29], we categorised the stress singularity for PTT and Giesekus fluids in planar stick-slip flow. Here, we continue the investigation by presenting a numerical scheme for solving the full flow equations. Two distinct formulations of the constitutive equations are presented; one being the traditional Cartesian stress formulation (CSF) using a fixed Cartesian stress basis whilst the other is the natural stress formulation (NSF) which aligns the stress along streamlines. We use the schemes to verify the asymptotic results (Evans [30, 31] and Evans et al. [29]) at the singularity for the stress, velocity as well as the boundary layer structures at the wall (no-slip) and free (slip) surfaces. As for the re-entrant corner singularity (Renardy [32], Evans & Oishi [33, 34]), we show that the NSF can more accurately capture the behaviour near to the singularity than the CSF. This is also expected to be the case for die swell, where the free-surface is now able to deform.

There is only limited numerical work in the literature for the stick-slip flow of the PTT fluid and apparently no investigation for Giesekus. PTT has been considered by Fortin et al. [35], Baaijens [36], Xue et al. [37] and Karapetsas & Tsamopoulos [38]. Fortin et al. [35] use a finite element method (FEM) and present results for the polymer normal stress in the direction of flow and in the absence of a solvent viscosity. Convergence is obtained upto a limiting Weissenberg number $\mathrm{Wi}_{\mathrm{crit}}$, which increases as the PTT model parameter ϵ increases ($\mathrm{Wi}_{\mathrm{crit}} = 2, 13$, and unlimited for $\epsilon = 0, 0.02, 0.25$ respectively). They state that similar results are obtained with a solvent viscosity, although provide no quantitative details. Baaijens [36] uses a discontinuous Galerkin FEM to solve the PTT model, with again no solvent viscosity, presenting results upto Deborah number De $= 87$ for a large PTT model parameter $\epsilon = 0.25$ and which reduce to De=25.5 for the UCM case of $\epsilon = 0$. Karapetsas & Tsamopoulos [38] give a FEM based on

a modified elastic-viscous split stress EVSS-G scheme, which they apply in both planar and cylindrical cases and to the linear and exponential forms of the PTT model. Estimates of the elastic stress singularity are given, although these are almost exclusively for the no solvent viscosity case. There is a solitary result for a solvent viscosity fraction $\beta = 1/9$ for the exponential PTT model. However, in all the cases where they have numerical results, theoretical knowledge of the singularity is currently unknown. It is only for the linear PTT model with solvent viscosity that the singularity has so far been classified. Our results here then extend the literature by considering the linear PTT model in a solvent viscosity, as well as presenting the analogous results for Giesekus. Moreover, we present a transient scheme, which should be contrasted to all previous schemes which deal only with the steady situation.

The layout of the paper is as follows. The CSF and NSF of the PTT and Giesekus equations are presented in section 2 including the flow geometry, mesh description and the overview of the numerical methods. In section 3, we present the numerical convergence results for both formulations, including temporal convergence studies and profile analyses. The stress singularity investigation is conducted in Section 4. Not only are the stress singularities numerically verified, but also the theoretical boundary layer structures at both the stick and slip surfaces. Whilst the known theoretical asymptotic results at the singularity are technically valid as long as a solvent viscosity is present in the models, capturing the singularity numerically becomes extremely challenging as the solvent viscosity reduces. Results for $\beta = 1/9$, illustrating this are presented in section 4.3. Finally, the influence of Weissenberg number is investigated in section 4.4.

2 Flow equations

The geometry and governing equations relevant to this flow are described in [29]. The flow is incompressible with the extra-stress tensor being rheologically decomposed into solvent and polymer components while the geometry used in all simulations is illustrated in Fig. 1. The channel half-width H and mean speed V of the incoming flow are used as characteristic length and velocity scalings, whilst the pressure and both the solvent and polymer extra-stresses are all scaled using the total viscosity η (comprised of solvent η_s and polymer η_p)[1]. The dimensionless form of the flow equations are

$$\nabla \cdot \mathbf{v} = 0, \tag{2.1}$$

$$\mathrm{Re}\left(\frac{\partial \mathbf{v}}{\partial t} + \mathbf{v}\cdot\nabla\mathbf{v}\right) = -\nabla p + \beta\nabla^2\mathbf{v} + \nabla\cdot\mathbf{T}, \tag{2.2}$$

$$\mathbf{T} + \mathrm{Wi}\left(\overset{\triangledown}{\mathbf{T}} + \frac{\kappa}{(1-\beta)}\mathbf{g}(\mathbf{T})\right) = 2\,(1-\beta)\,\mathbf{D}, \tag{2.3}$$

$$\mathbf{g}(\mathbf{T}) = \begin{cases} \mathrm{tr}(\mathbf{T})\mathbf{T}, & \text{PTT}, \\ \mathbf{T}^2, & \text{Giesekus}, \end{cases} \tag{2.4}$$

with $\mathbf{D} = \frac{1}{2}(\nabla\mathbf{v} + (\nabla\mathbf{v})^T)$ the rate-of-strain tensor and the upper-convected stress derivative defined as

$$\overset{\triangledown}{\mathbf{T}} = \frac{\partial \mathbf{T}}{\partial t} + (\mathbf{v}\cdot\nabla)\,\mathbf{T} - (\nabla\mathbf{v})\,\mathbf{T} - \mathbf{T}\,(\nabla\mathbf{v})^T. \tag{2.5}$$

The dimensionless parameters are the Reynolds number Re, Weissenberg number Wi and retardation parameter $\beta \in [0,1]$ (the dimensionless retardation time or dimensionless solvent viscosity). The model parameter κ is the coefficient of the quadratic stress terms representing the PTT model parameter (ϵ being commonly used) or Giesekus mobility factor.

In component form relative to fixed Cartesian axes, Eqs. (2.1)-(2.3) can be re-written as

[1] We remark that this is an alternative non-dimenionsalisation for the extra-stresses to that presented in [29] which used the respective solvent and polymer viscosities instead of the total viscosity.

$$\frac{\partial u}{\partial x}+\frac{\partial v}{\partial y}=0, \tag{2.6}$$

$$\mathrm{Re}\left(\frac{\partial u}{\partial t}+u\frac{\partial u}{\partial x}+v\frac{\partial u}{\partial y}\right)=-\frac{\partial p}{\partial x}+\beta\left(\frac{\partial^2 u}{\partial x^2}+\frac{\partial^2 u}{\partial y^2}\right)+\frac{\partial T_{11}}{\partial x}+\frac{\partial T_{12}}{\partial y}, \tag{2.7}$$

$$\mathrm{Re}\left(\frac{\partial v}{\partial t}+u\frac{\partial v}{\partial x}+v\frac{\partial v}{\partial y}\right)=-\frac{\partial p}{\partial y}+\beta\left(\frac{\partial^2 v}{\partial x^2}+\frac{\partial^2 v}{\partial y^2}\right)+\frac{\partial T_{12}}{\partial x}+\frac{\partial T_{22}}{\partial y}, \tag{2.8}$$

$$T_{11}+\mathrm{Wi}\left(\frac{\partial T_{11}}{\partial t}+u\frac{\partial T_{11}}{\partial x}+v\frac{\partial T_{11}}{\partial y}-2\frac{\partial u}{\partial x}T_{11}-2\frac{\partial u}{\partial y}T_{12}+\frac{\kappa}{(1-\beta)}g_{11}\right)=2\left(1-\beta\right)\frac{\partial u}{\partial x}, \tag{2.9}$$

$$T_{22}+\mathrm{Wi}\left(\frac{\partial T_{22}}{\partial t}+u\frac{\partial T_{22}}{\partial x}+v\frac{\partial T_{22}}{\partial y}-2\frac{\partial v}{\partial y}T_{22}-2\frac{\partial v}{\partial x}T_{12}+\frac{\kappa}{(1-\beta)}g_{22}\right)=2\left(1-\beta\right)\frac{\partial v}{\partial y}, \tag{2.10}$$

$$T_{12}+\mathrm{Wi}\left(\frac{\partial T_{12}}{\partial t}+u\frac{\partial T_{12}}{\partial x}+v\frac{\partial T_{12}}{\partial y}-\frac{\partial v}{\partial x}T_{11}-\frac{\partial u}{\partial y}T_{22}+\frac{\kappa}{(1-\beta)}g_{12}\right)=(1-\beta)\left(\frac{\partial u}{\partial y}+\frac{\partial v}{\partial x}\right), \tag{2.11}$$

where Eq. (2.4) is now defined as

$$g_{11}=\begin{cases}\left(T_{11}+T_{22}\right)T_{11}, & \text{PTT},\\ \left(T_{11}^2+T_{12}^2\right), & \text{Giesekus},\end{cases} \tag{2.12}$$

$$g_{12}=\left(T_{11}+T_{22}\right)T_{12} \tag{2.13}$$

$$g_{22}=\begin{cases}\left(T_{11}+T_{22}\right)T_{22}, & \text{PTT},\\ \left(T_{12}^2+T_{22}^2\right), & \text{Giesekus}.\end{cases} \tag{2.14}$$

We refer to (2.9)–(2.11) as the Cartesian stress formulation of the constitutive equation. An alternative is to align the polymer stress basis along streamlines, thus introducing natural stress variables. We follow closely here the construction of Renardy [32] (see also [39] and [40]). Introducing the configuration tensor $\mathbf{A}$ by

$$\mathbf{T}=\frac{(1-\beta)}{\mathrm{Wi}}\left(\mathbf{A}-\mathbf{I}\right), \tag{2.15}$$

the polymer constitutive equation (2.3) becomes

$$\mathrm{Wi}\ \overset{\triangledown}{\mathbf{A}}+\left(\mathbf{A}-\mathbf{I}\right)+\kappa\mathbf{g}\left(\mathbf{A}-\mathbf{I}\right)=0, \tag{2.16}$$

after using $\overset{\triangledown}{\mathbf{I}}=-2\mathbf{D}$. We now express $\mathbf{A}$ in terms of the dyadic products of $\mathbf{v}$ and an orthogonal vector $\mathbf{w}$ as follows

$$\mathbf{A}=\lambda\mathbf{v}\mathbf{v}^T+\mu\left(\mathbf{v}\mathbf{w}^T+\mathbf{w}\mathbf{v}^T\right)+\nu\mathbf{w}\mathbf{w}^T, \tag{2.17}$$

where

$$\mathbf{v}=\left(u,v\right)^T, \qquad \mathbf{w}=\frac{1}{|\mathbf{v}|^2}\left(-v,u\right)^T,$$

with $\mathbf{w}$ chosen such that $|\mathbf{v}\times\mathbf{w}|=1$. Computationally, it is convenient to use scaled natural stress variables $\hat{\lambda},\hat{\mu},\hat{\nu}$ as follows

$$\lambda=\frac{\hat{\lambda}}{|\mathbf{v}|^2}, \qquad \mu=\hat{\mu}, \quad \nu=\hat{\nu}|\mathbf{v}|^2, \tag{2.18}$$

which satisfy the following component equations

$$\mathrm{Wi}\left[\frac{\partial\hat{\lambda}}{\partial \mathrm{t}}+\frac{2\hat{\mu}}{|\mathbf{v}|^2}\left(\mathrm{v}\frac{\partial \mathrm{u}}{\partial \mathrm{t}}-\mathrm{u}\frac{\partial \mathrm{v}}{\partial \mathrm{t}}\right)+|\mathbf{v}|^2(\mathbf{v}\cdot\nabla)\left(\frac{\hat{\lambda}}{|\mathbf{v}|^2}\right)+2\hat{\mu}|\mathbf{v}|^2\nabla\cdot\mathbf{w}\right]+\left(\hat{\lambda}-1\right)+\kappa \mathrm{g}_{\hat{\lambda}}=0, \tag{2.19}$$

$$\mathrm{Wi}\left[\frac{\partial\hat{\mu}}{\partial \mathrm{t}}+\left(\frac{\hat{\lambda}-\hat{\nu}}{|\mathbf{v}|^2}\right)\left(\mathrm{u}\frac{\partial \mathrm{v}}{\partial \mathrm{t}}-\mathrm{v}\frac{\partial \mathrm{u}}{\partial \mathrm{t}}\right)+(\mathbf{v}\cdot\nabla)\hat{\mu}+\hat{\nu}|\mathbf{v}|^2\nabla\cdot\mathbf{w}\right]+\hat{\mu}+\kappa \mathrm{g}_{\hat{\mu}}=0, \tag{2.20}$$

$$\mathrm{Wi}\left[\frac{\partial\hat{\nu}}{\partial \mathrm{t}}+\frac{2\hat{\mu}}{|\mathbf{v}|^2}\left(\mathrm{u}\frac{\partial \mathrm{v}}{\partial \mathrm{t}}-\mathrm{v}\frac{\partial \mathrm{u}}{\partial \mathrm{t}}\right)+\frac{1}{|\mathbf{v}|^2}(\mathbf{v}\cdot\nabla)\left(\hat{\nu}|\mathbf{v}|^2\right)\right]+(\hat{\nu}-1)+\kappa \mathrm{g}_{\hat{\nu}}=0, \tag{2.21}$$

where

$$g_{\hat{\lambda}}=\begin{cases}\left(\hat{\lambda}+\hat{\nu}-2\right)\left(\hat{\lambda}-1\right), & \text{PTT},\\ \left[\left(\hat{\lambda}-1\right)^2+\hat{\mu}^2\right], & \text{Giesekus},\end{cases} \tag{2.22}$$

$$g_{\hat{\mu}}=\left(\hat{\lambda}+\hat{\nu}-2\right)\hat{\mu} \tag{2.23}$$

$$g_{\hat{\nu}}=\begin{cases}\left(\hat{\lambda}+\hat{\nu}-2\right)(\hat{\nu}-1), & \text{PTT},\\ \left[(\hat{\nu}-1)^2+\hat{\mu}^2\right], & \text{Giesekus}\end{cases} \tag{2.24}$$

with

$$|\mathbf{v}|^2\nabla.\mathbf{w}=|\mathbf{v}|^2\left(\frac{\partial}{\partial x}\left(-\frac{v}{|\mathbf{v}|^2}\right)+\frac{\partial}{\partial y}\left(\frac{u}{|\mathbf{v}|^2}\right)\right)=\frac{1}{|\mathbf{v}|^2}\left((v^2-u^2)\left(\frac{\partial v}{\partial x}+\frac{\partial u}{\partial y}\right)+4uv\frac{\partial u}{\partial x}\right).$$

The component form of (2.15), adopting eqs. (2.17) and (2.18) results in the following equations

$$T_{11}=\frac{(1-\beta)}{\mathrm{Wi}}\left(-1+\frac{1}{|\mathbf{v}|^2}\left(\hat{\lambda}u^2-2\hat{\mu}uv+\hat{\nu}v^2\right)\right), \tag{2.25}$$

$$T_{12}=\frac{(1-\beta)}{\mathrm{Wi}|\mathbf{v}|^2}\left(\hat{\lambda}uv+\hat{\mu}(u^2-v^2)-\hat{\nu}uv\right), \tag{2.26}$$

$$T_{22}=\frac{(1-\beta)}{\mathrm{Wi}}\left(-1+\frac{1}{|\mathbf{v}|^2}\left(\hat{\lambda}v^2+2\hat{\mu}uv+\hat{\nu}u^2\right)\right), \tag{2.27}$$

with the inverse relationships being

$$\hat{\lambda}-1=\frac{\mathrm{Wi}}{(1-\beta)|\mathbf{v}|^2}\left(u^2T_{11}+2uvT_{12}+v^2T_{22}\right), \tag{2.28}$$

$$\hat{\mu}=\frac{\mathrm{Wi}}{(1-\beta)|\mathbf{v}|^2}\left(-uvT_{11}+(u^2-v^2)T_{12}+uvT_{22}\right), \tag{2.29}$$

$$\hat{\nu}-1=\frac{\mathrm{Wi}}{(1-\beta)|\mathbf{v}|^2}\left(v^2T_{11}-2uvT_{12}+u^2T_{22}\right). \tag{2.30}$$

We refer to (2.19)–(2.21) as the natural stress formulation (NSF) of the constitutive equations, which may be solved with the momentum equation in the form (2.7)–(2.8) on using (2.25)–(2.27).

2.1 Flow description

The planar stick-slip geometry is shown schematically in Figure 1. We have a sudden modification in the boundary condition at the stick-slip transition point where the stress singularity is located. On the solid surface (denoted here as $\partial\Omega_{st}$), we have no-slip boundary condition:

$$\mathbf{v}=\mathbf{0} \quad \text{in} \quad \partial\Omega_{st}, \tag{2.31}$$

whilst, on the slip surface $\partial\Omega_{sl}$, we have no flow across the surface,

$$v = 0 \quad \text{in} \quad \partial\Omega_{sl} \tag{2.32}$$

and no shear-stress

$$T_{12} + \beta\frac{\partial u}{\partial y} = 0 \quad \text{on} \quad \partial\Omega_{sl}. \tag{2.33}$$

The boundary conditions for the velocity field imposed at the inlet assumes fully developed flow ($u = u(y), v = 0$), whilst a Neumann homogeneous boundary condition is applied at the outlet. As an initial condition at $t = 0$, the Cartesian extra stress is set as $\mathbf{T} = 0$.

The initial and boundary conditions for the natural stress variables $\hat{\lambda}$, $\hat{\mu}$ and $\hat{\nu}$ are taken consistent with the Cartesian extra stress variables using (2.28)-(2.30). At the inlet, with $v = 0$ for fully developed flow, we have

$$\hat{\lambda} = \left[\frac{\mathrm{Wi}}{(1-\beta)}T_{11} + 1\right]/u^2, \qquad \hat{\mu} = \frac{\mathrm{Wi}}{(1-\beta)}T_{12}, \qquad \hat{\nu} = u^2\left[\frac{\mathrm{Wi}}{(1-\beta)}T_{22} + 1\right], \tag{2.34}$$

whilst at the outlet, a homogeneous Neumann condition is employed for the NS variables. For the stick and slip regions, the conditions (2.31), (2.32) are adopted togther with the equivalent of (2.33) being

$$\frac{(1-\beta)}{\mathrm{Wi}}\hat{\mu} + \beta\frac{\partial u}{\partial y} = 0 \quad \text{on} \quad \partial\Omega_{sl}. \tag{2.35}$$

The initialisation $\hat{\lambda} = \hat{\nu} = 1$ and $\hat{\mu} = 0$ at $t = 0$ completes the specification of the NS variables.

We remark that at the inlet (and also initially at $t = 0$), specifying the three Cartesian extra-stresses or the three natural stress variables is sufficient to determine the two characteristic quantities required for well-posedness of the PDE system (2.1)–(2.3) [41, 42]. The two characteristic quantities here are

$$\det\left(\mathbf{T} + \frac{(1-\beta)}{\mathrm{Wi}}\mathbf{I}\right) = \frac{(1-\beta)^2}{\mathrm{Wi}^2}(\hat{\lambda}\hat{\nu} - \hat{\mu}^2),$$

and

$$(\mathbf{v}^{\perp})^T\left(\mathbf{T} + \frac{(1-\beta)}{\mathrm{Wi}}\mathbf{I}\right)\mathbf{v}^{\perp} = \frac{(1-\beta)}{\mathrm{Wi}}|\mathbf{v}|^2\hat{\nu},$$

where $\mathbf{v}^{\perp} = |\mathbf{v}|^2\mathbf{w}$, which are transported along the characteristics associated with the constitutive equation (2.3). In the steady case, the characteristics are streamlines, whilst they are particle paths in the unsteady case. The classification analysis of [41, 42] for the UCM model, still pertains for the PTT and Giesekus models in the forms presented here, although the transport equations for the characteristic quantities necessarily change.

2.2 Overview of the numerical method

We implement the numerical scheme in a finite-difference framework. The algorithm has two main steps:

1. Computation of velocity and pressure fields. Based on a semi-implicit scheme, Eqs. (2.1) and (2.2) are uncoupled via an incremental projection method [43]. In this strategy, the momentum equation (2.2) is solved for a tentative velocity field $\widetilde{\mathbf{v}}^{(n+1)}$ considering an implicit discretization for the viscous term while the convective terms, pressure gradient and divergence of the stress tensor are treated in an explicit manner, e.g,

$$\frac{\widetilde{\mathbf{v}}^{(n+1)}}{\delta t} - \frac{\beta}{Re}\nabla^2\widetilde{\mathbf{v}}^{(n+1)} = \frac{\mathbf{v}^{(n)}}{\delta t} - ((\mathbf{v}\cdot\nabla)\mathbf{v})^{(n)} - \frac{1}{Re}\nabla p^{(n)} + \frac{1}{Re}\nabla\cdot(\mathbf{T})^{(n)}, \tag{2.36}$$

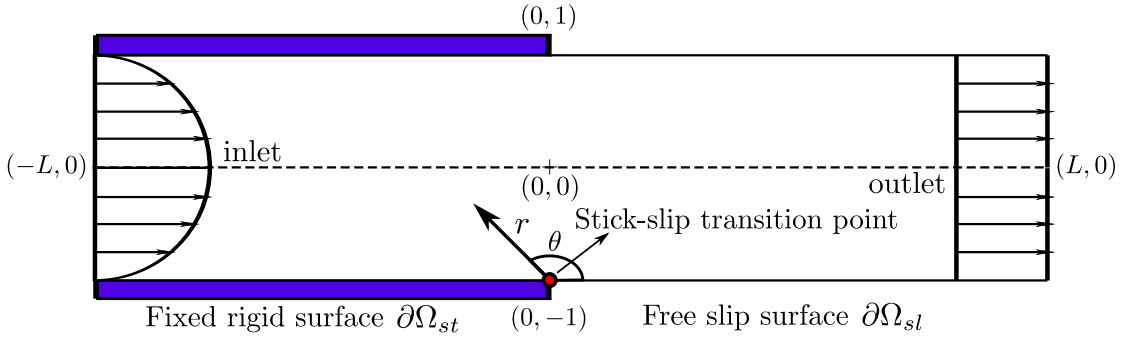

Figure 1: The stick-slip geometry description. The $(0,-1)$ point represents the stick-slip transition point. The dimensionless domain half-length L is typically taken as 8.

where δt is the time-step. Once the intermediate velocity field is obtained, the final velocity field is updated based on the Helmholtz-Hodge decomposition [44]

$$\mathbf{v}^{(n+1)} = \widetilde{\mathbf{v}}^{(n+1)} - \nabla\phi^{(n+1)}, \tag{2.37}$$

where the final pressure field is incremented by an iterative process [45, 46]

$$p^{(n+1)} = p^{(n)} + \frac{Re}{\delta t}\phi^{(n+1)}, \tag{2.38}$$

with ϕ being an intermediate pressure which needs to be previously computed. This computation is done by solving the Poisson-like equation

$$\nabla^2\phi^{(n+1)} = \nabla\cdot\widetilde{\mathbf{v}}^{(n+1)}. \tag{2.39}$$

To solve the stick-slip problem by the incremental projection method, it is necessary to construct correct boundary conditions for ϕ, respecting the boundary conditions imposed for the velocity field $\mathbf{v}$ in the two regions of the domain:

- Boundary conditions for the Poisson equation in the stick region: As the no-slip boundary condition applies for the velocity field, we have imposed the classical homogeneous Neumann boundary condition for the intermediate pressure, i.e.

$$\frac{\partial\phi}{\partial y} = 0 \quad \text{in} \quad \partial\Omega_{st}. \tag{2.40}$$

- Boundary conditions for the Poisson equation in the slip region: We propose a specific boundary condition for the intermediate pressure when the projection method is applied under slip conditions. The normal stress condition is

$$\mathbf{n}\cdot[-p\mathbf{I} + 2\beta\mathbf{D} + \mathbf{T}]\cdot\mathbf{n}^T = 0, \tag{2.41}$$

where $\mathbf{n}$ denotes the outward unit normal vector to the boundary $\partial\Omega_{sl}$. Equation (2.41) is commonly used as a free surface boundary condition for solving interface problems (see in [47]). Imposing Eq. (2.41) on the free slip surface and considering the fixed normal vector $\mathbf{n} = [0,\ \ 1]$, we obtain:

$$-p + 2\beta\frac{\partial v}{\partial y} + T_{22} = 0. \tag{2.42}$$

Using the continuity equation (2.6), (2.42) may be rewritten as

$$-p - 2\beta\frac{\partial u}{\partial x} + T_{22} = 0. \tag{2.43}$$

According to the ideas of the semi-implicit version of the Marker-And-Cell algorithm [43], Eq. (2.43) can be used to compute the pressure field at the free surface by an iterative process imposing the following time discretization:

$$-p^{(n+1)} = 2\beta \frac{\partial u^{(n+1)}}{\partial x} - T_{22}^{(n)}. \tag{2.44}$$

In the present work, Eq. (2.44) is combined with the update velocity (2.37) and pressure (2.38), resulting in a specific boundary condition for ϕ on the free slip surface:

$$\frac{Re}{\delta t}\phi^{(n+1)} - 2\beta \frac{\partial^2 \phi^{(n+1)}}{\partial x^2} = -2\beta \frac{\partial \widetilde{u}^{(n+1)}}{\partial x} + T_{22}^{(n)} - p^{(n)} \quad \text{in} \quad \partial\Omega_{sl}. \tag{2.45}$$

2. Computation of the non-Newtonian tensor. After obtaining the final velocity and pressure fields, the final value for the extra stress tensor $\mathbf{T}^{(n+1)}$ is computed according to the two stress formulation:

- Cartesian Stress Formulation. Equation (2.3) is discretized in the following explicit manner:

$$\begin{aligned}\frac{\mathbf{T}^{(n+1)} - \mathbf{T}^{(n)}}{\delta t} &= \frac{1}{Wi}\left(-\mathbf{T}^{(n)} + \left(\nabla \mathbf{v}^{(n+1)} + \left(\nabla \mathbf{v}^{(n+1)}\right)^T\right)\right) \\ &- \left(\mathbf{v}^{(n+1)} \cdot \nabla\right)\mathbf{T}^{(n)} + \left(\nabla \mathbf{v}^{(n+1)}\right)\mathbf{T}^{(n)} + \mathbf{T}^{(n)}\left(\nabla \mathbf{v}^{(n+1)}\right)^T - \frac{\kappa}{1-\beta}\mathbf{g}(\mathbf{T}^{(n)}) + 2\frac{1-\beta}{Wi}\mathbf{D}^{(n)},\end{aligned} \tag{2.46}$$

where $\mathbf{g}(\mathbf{T}^{(n)})$ is constructed selecting the fluid model as was described in Eq. (2.4). Therefore, the components $(T_{11}^{n+1}, T_{12}^{n+1}, T_{22}^{n+1})$ are then computed directly from Eq. (2.46).

- Natural Stress Formulation. The first stage for this formulation is the solution of Eqs. (2.19)–(2.21) using an explicit time discretization. For example, Eq. (2.19) can be written as

$$\begin{aligned}\frac{\hat{\lambda}^{(n+1)} - \hat{\lambda}^{(n)}}{\delta t} &= -\frac{1}{\mathrm{Wi}}\left(\hat{\lambda}^{(n)} - 1\right) - \kappa g_{\hat{\lambda}^{(n)}} - 2\hat{\mu}^{(n)}|\mathbf{v}^{(n+1)}|^2 \nabla \cdot \mathbf{w}^{(n+1)} \\ &- \frac{2\hat{\mu}^{(n)}}{(|\mathbf{v}^{(n+1)}|^2 + \mathrm{tol})}\left(v^{(n+1)}\frac{u^{(n+1)} - u^{(n)}}{\delta t} - u^{(n+1)}\frac{v^{(n+1)} - v^{(n)}}{\delta t}\right) \\ &- |\mathbf{v}^{(n+1)}|^2 (\mathbf{v}^{(n+1)} \cdot \nabla)\left(\frac{\hat{\lambda}^{(n)}}{(|\mathbf{v}^{(n+1)}|^2 + \mathrm{tol})}\right),\end{aligned} \tag{2.47}$$

where

$$\begin{aligned}|\mathbf{v}^{(n+1)}|^2 \nabla . \mathbf{w}^{(n+1)} &= \frac{1}{|\mathbf{v}^{(n+1)}|^2 + \mathrm{tol}}\left(((v^{(n+1)})^2 - (u^{(n+1)})^2)\left(\frac{\partial v^{(n+1)}}{\partial x} + \frac{\partial u^{(n+1)}}{\partial y}\right)\right. \\ &\left. + 4u^{(n+1)}v^{(n+1)}\frac{\partial u^{(n+1)}}{\partial x}\right).\end{aligned} \tag{2.48}$$

The tolerance $\mathrm{tol} = 10^{-6}$ is imposed for regularization in order to avoid numerical division by zero in domain regions where the velocity field vanishes [33]. Equations (2.20) and (2.21) are discretized in a similar manner, resulting in the values for $\hat{\mu}^{(n+1)}$ and $\hat{\nu}^{(n+1)}$. Obtained the NS variables in level time $(n+1)$ we can use the relationships Eqs. (2.25)–(2.27) to compute the final components $(T_{11}^{n+1}, T_{12}^{n+1}, T_{22}^{n+1})$ of the extra-stress tensor.

The algorithms of the numerical schemes for CSF and NSF are summarized in the flowchart in Fig 2.

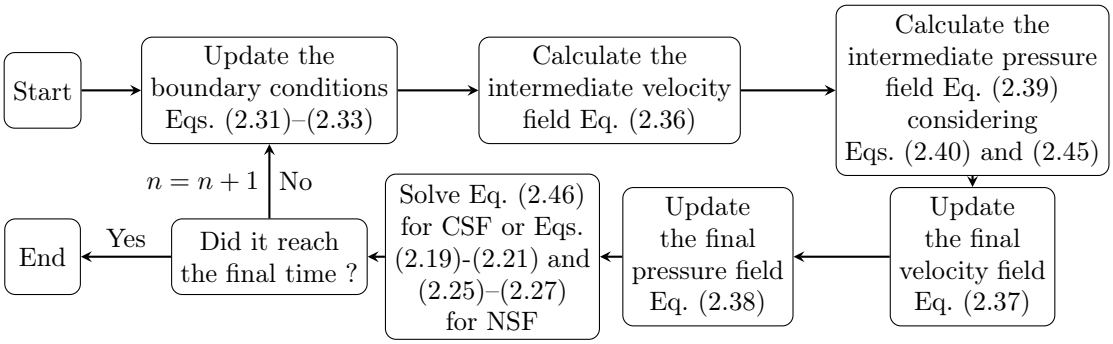

Figure 2: Flowchart of the numerical schemes.

2.3 Non-uniform mesh discretization

To capture the effect of the singularity, we have applied a stretching strategy for refining the mesh elements around the stick-slip transition point, as illustrated in Fig. 3. In particular, we use three non-uniform meshes, M1, M2 and M3. Details for the minimum value for the space steps Δx_{min} and Δy_{min} being given in Table 1.

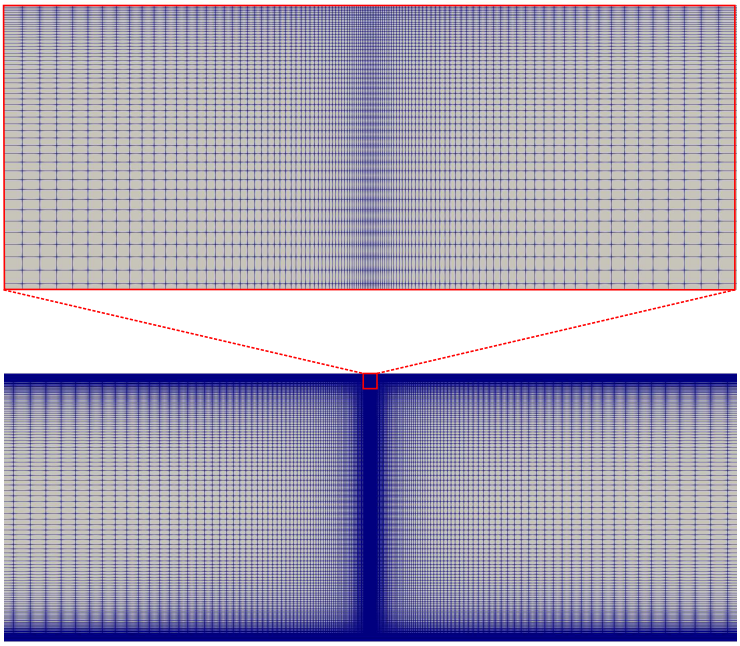

Figure 3: Visualization details of the non-uniform mesh for the stick-slip problem.

Table 1: Meshes used in the present work.

Mesh	Δx_{min}	Δy_{min}
M1	5.0×10^{-3}	5.0×10^{-3}
M2	5.0×10^{-4}	5.0×10^{-4}
M3	5.0×10^{-5}	5.0×10^{-5}

3 Convergence results

We demonstrate the capability of the numerical scheme for solving the stick-slip problem by considering the complete system of governing equations for the PTT and Giesekus models using both the Cartesian and natural stress formulations. We first validate the scheme through a mesh refinement study by considering profiles of the pressure, first normal stress difference and velocity in two cross sections of the domain. After this, we compare numerical results for the polymer stress near the singularity with the predicted theoretical asymptotic behaviours. In all simulations in this Section, we use parameter values of $Re = 0.01$, $Wi = 1$, $\kappa = 0.1$ and $\beta = 1/2$.

The verification of the numerical schemes for Newtonian flow can be found in the Appendix A.

3.1 Numerical study of temporal convergence

Here we confirm temporal convergence of the schemes as the time step reduces. Since the main purpose of the current work is related to the numerical behaviour of variables around the singularity, temporal convergence is studied through the local residual as a time function. In particular, the local residuals are captured in a control point located in the closest cell of the singularity.

The local residuals for the velocity in the x direction, the component 11 of the extra stress tensor and the $\hat{\lambda}$ NS variable are respectively evaluated as

$$\begin{aligned} res(u)|_P = & \left.\frac{u^{(n+1)} - u^{(n)}}{\delta t}\right|_P + \left.\left(u\frac{\partial u}{\partial x} + v\frac{\partial u}{\partial y}\right)\right|_P^{(n+1)} + \left.\frac{1}{\mathrm{Re}}\,\frac{\partial p}{\partial x}\right|_P^{(n+1)} - \left.\frac{\beta}{\mathrm{Re}}\left(\frac{\partial^2 u}{\partial x^2} + \frac{\partial^2 u}{\partial y^2}\right)\right|_P^{(n+1)} \\ & - \left.\frac{1}{\mathrm{Re}}\left(\frac{\partial T_{11}}{\partial x} - \frac{\partial T_{12}}{\partial y}\right)\right|_P^{(n+1)} \end{aligned} \tag{3.49}$$

$$\begin{aligned} res(T_{11})|_P = & \left.\frac{T_{11}^{(n+1)} - T_{11}^{(n)}}{\delta t}\right|_P + \left.\left(u\frac{\partial T_{11}}{\partial x} + v\frac{\partial T_{11}}{\partial y}\right)\right|_P^{(n+1)} - \left.\left(2\frac{\partial u}{\partial x}T_{11} + 2\frac{\partial u}{\partial y}T_{12}\right)\right|_P^{(n+1)} \\ & + \left.\frac{\kappa}{(1-\beta)}g_{11}\right|_P^{(n+1)} - \left.\frac{2}{\mathrm{Wi}}(1-\beta)\,\frac{\partial u}{\partial x}\right|_P^{(n+1)}, \end{aligned} \tag{3.50}$$

and

$$\begin{aligned} res(\hat{\lambda})|_P = & \left.\frac{\hat{\lambda}^{(n+1)} - \hat{\lambda}^{(n)}}{\delta t}\right|_P + \left.\left(\frac{2\hat{\mu}}{|\mathbf{v}|^2}\left(v\frac{\partial u}{\partial t} - u\frac{\partial v}{\partial t}\right)\right)\right|_P^{(n+1)} + \left.\left(|\mathbf{v}|^2(\mathbf{v}\cdot\nabla)\left(\frac{\hat{\lambda}}{|\mathbf{v}|^2}\right)\right)\right|_P^{(n+1)} \\ & + \left.\left(2\hat{\mu}|\mathbf{v}|^2\nabla\cdot\mathbf{w}\right)\right|_P^{(n+1)} + \left.\left(\frac{1}{\mathrm{Wi}}\left(\hat{\lambda} - 1\right) + \frac{\kappa}{\mathrm{Wi}}g_{\hat{\lambda}}\right)\right|_P^{(n+1)}, \end{aligned} \tag{3.51}$$

where g_{11} is computed from Eq. (2.12) while $g_{\hat{\lambda}}$ is obtained from Eq. (2.22). The local residuals for the other components of the extra stress tensor and for the remaining NS variables can be constructed in a similar manner. In particular, the local residual investigation will be done considering only the PTT model (results for Giesekus being similar) on the coarse mesh M1 varying the time-step as $\delta t = 5 \times 10^{-4}, 1 \times 10^{-4}, 5 \times 10^{-5}, 1 \times 10^{-5}$.

Figures 4 and 5 present the time variation of local residuals on a logarithm scale for CSF and NSF respectively. They confirm temporal convergence for both formulations, provided a sufficiently small time-step of $\delta t = 1 \times 10^{-4}$ or smaller is used. However, for the largest time step shown, $\delta t = 5 \times 10^{-4}$, the local residual for Eq. (3.49) is still large compared to those of the smaller time-steps and in fact, the use of a time-step greater than $\delta t = 5 \times 10^{-4}$ leads to a complete breakdown of the code for both formulations. Therefore, in order to capture the expected behaviour of the stress singularities, in this work we have adopted small time step values for all meshes, for instance $\delta t = 1 \times 10^{-5}$ for M2 and $\delta t = 5 \times 10^{-6}$ for M3. As a consequence of this CFL limitation, the CPU time can considerably increase in the application of very refined meshes, such as those used in [38] in the steady case. Interestingly, these residual plots also illustrate the significant rate of convergence improvement for the NS variables over the CS variables, emphasising that the two formulations behave in fundamentally different ways.

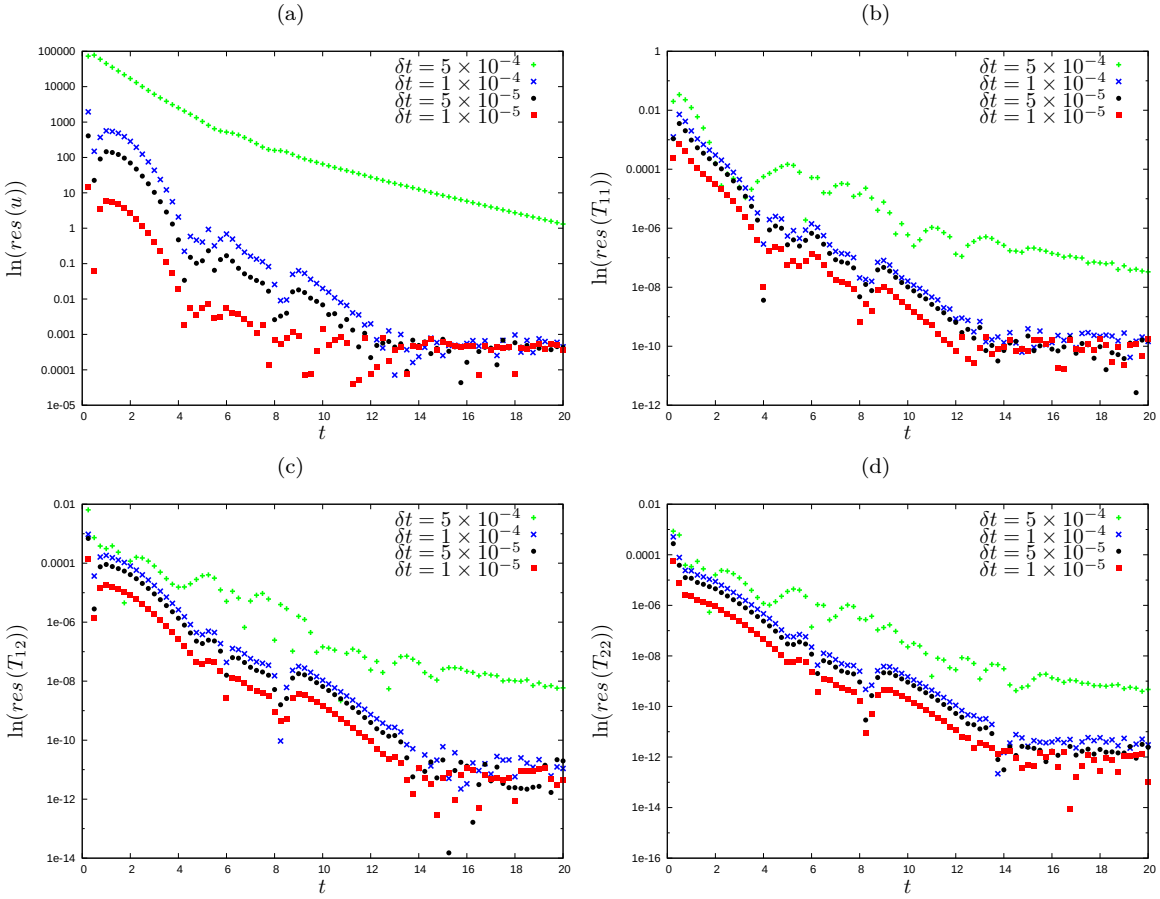

Figure 4: Time variation of the CSF local residuals of (a) u, (b) T_{11}, (c) T_{12} and (d) T_{22} near to the singularity for the PTT model using $\beta = 1/2$.

3.2 Numerical investigation of the profiles

Initially, we confirm temporal convergence for the velocity component u, the pressure field p and the first normal stress difference $N_1 = T_{11} - T_{22}$ along the line $y = 1$. Fig. 6 presents results for PTT using CSF on the coarse mesh M1 for the same time-steps adopted in the previous section. The temporal convergence behaviour for Giesekus is similar.

A mesh refinement study is now employed along the line $y = 1$ that contains the stick-slip transition point. Results for the velocity component u are presented in Figs. 7a) and b) for PTT and Giesekus,

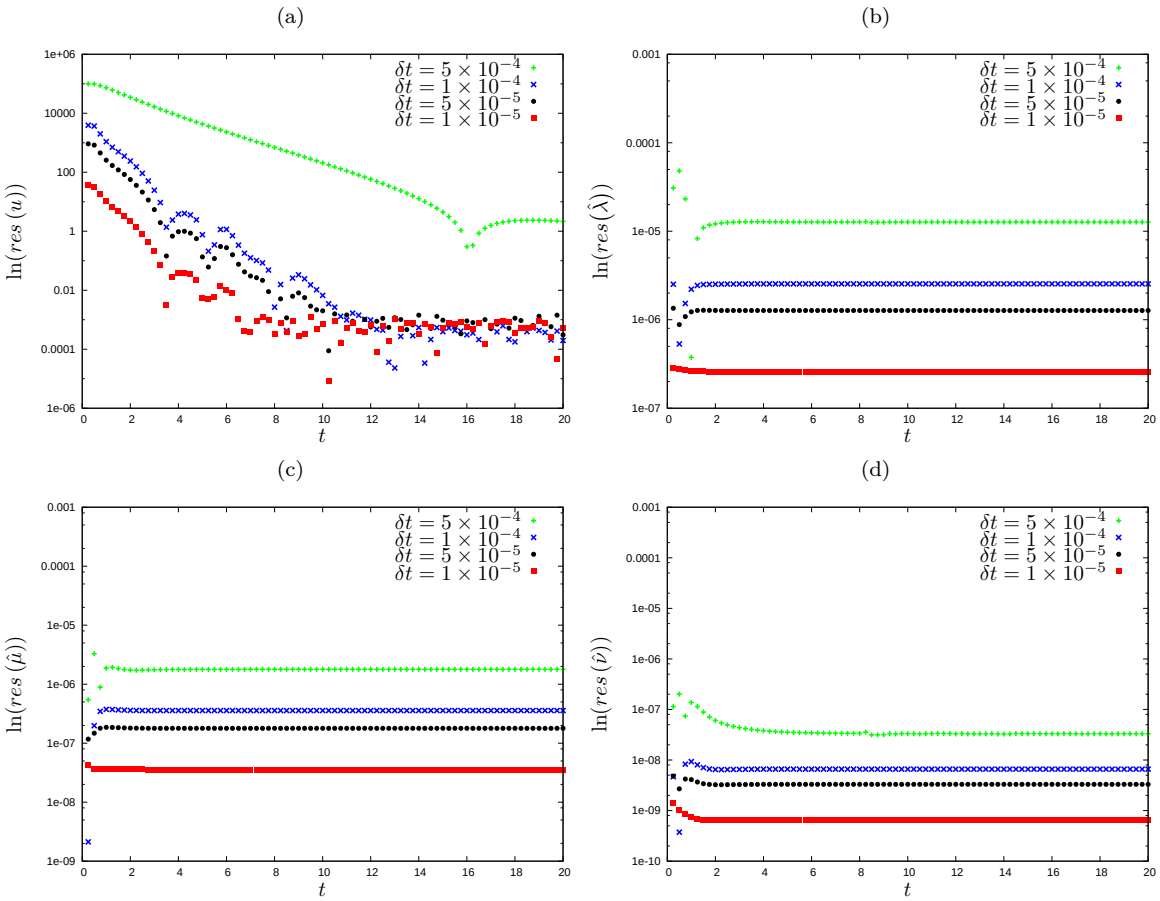

Figure 5: Time variation of the NSF local residuals of (a) u, (b) $\hat{\lambda}$, (c) $\hat{\mu}$ and (d) $\hat{\nu}$ near to the singularity for the PTT model using $\beta = 1/2$.

respectively. These figures illustrate numerical convergence of solutions for both formulations and for both fluids. In particular, for the u-velocity profile, no significant difference was observed between the CSF and NSF results.

The presence of the stick-slip separation or transition point at $y = 1$ is more evident for p and N_1, as can be seen in Figs. 7c) and d) and Figs. 7e) and f), respectively. Concerning the pressure field, a difference may be observed between the CSF and NSF results for both fluids at the free surface and around the stick-slip transition point where the minimum pressure is significantly lower for NSF in M3 than CSF. Figures 7e) and f) give the distribution of N_1 along the line $y = 1$. Far away of the stick slip transition point, the mesh refinement confirms the numerical convergence of the results for both models and formulations. However, around the singularity, the peak values of the first normal stress difference increase significantly as the mesh is refined. These behaviours are similar to those observed in [36,38] for the PTT model with $\beta = 0$.

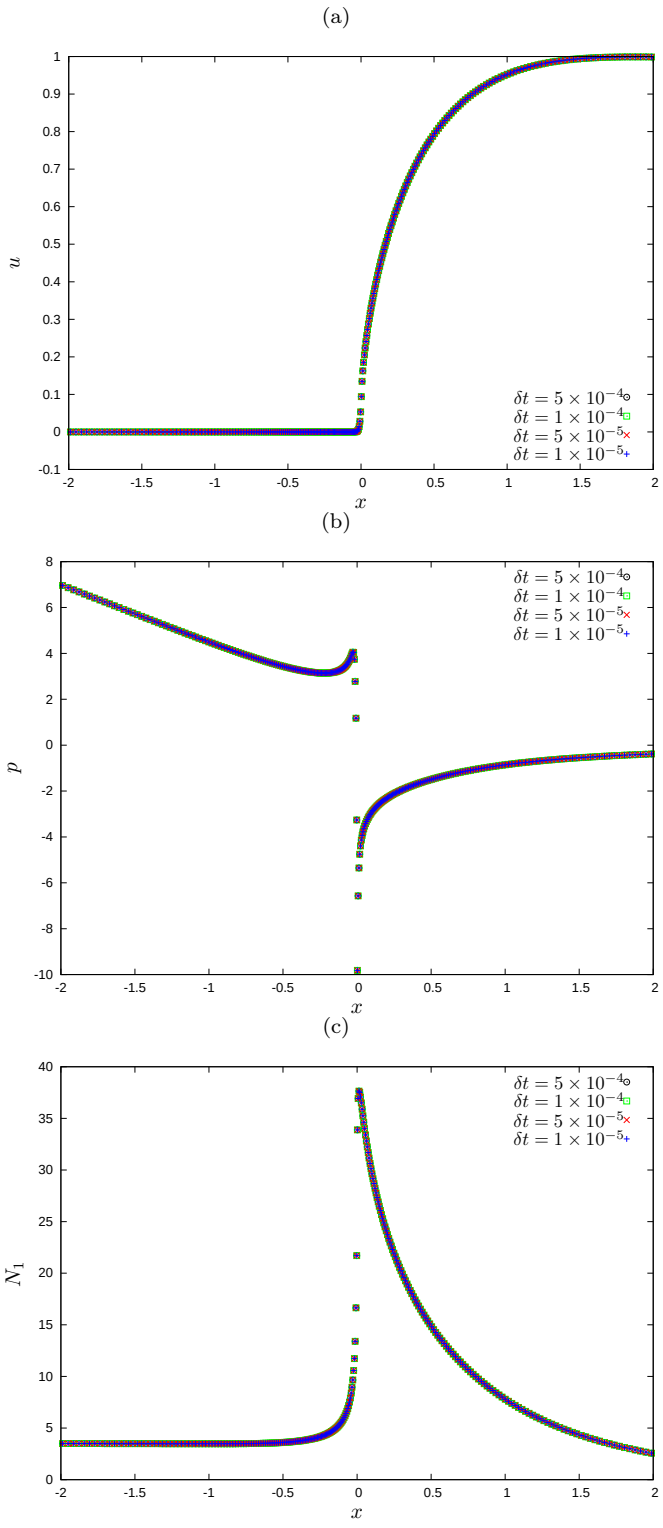

Figure 6: Profiles of (a) u, (b) p and (c) N_1 along the horizontal line $y = 1$ for the PTT model using different time steps.

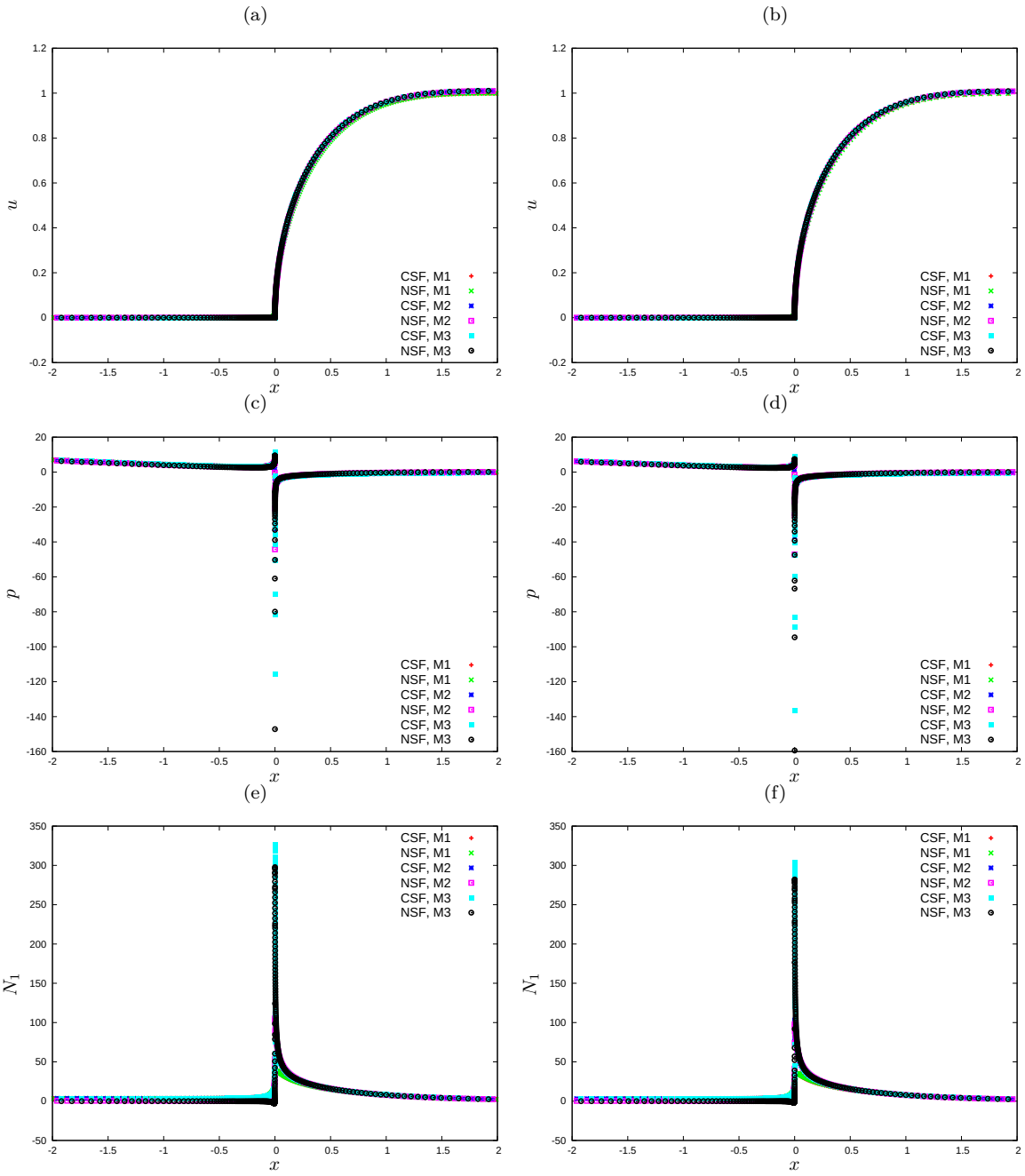

Figure 7: Profiles of (a) u (PTT), (b) u (Giesekus), (c) p (PTT) (d) p (Giesekus), (e) N_1 (PTT) and (f) N_1 (Giesekus) along the horizontal line $y = 1$.

4 Stress singularity results

In this Section, we initially verify the formulations comparing the numerical results with the asymptotic results, and after this, a numerical investigation of the boundary layers on the stick-slip problem is conducted. Moreover, we explore the results for small solvent viscosities. Finally, we have analysed the singularity results varying the Weissenberg number.

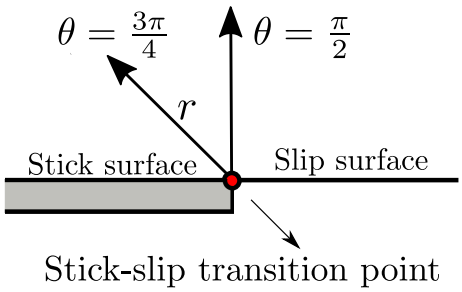

Figure 8: Illustration of the selected angles for studying the asymptotic behavior near the stick-slip transition point.

4.1 Numerical comparison with the asymptotic results

We now compare our results with the asymptotic results of Evans et al. [29] considering fixed values of Weissenberg number, $Wi = 1$, and the viscosity ratio, $\beta = 1/2$. In summary, the solvent stress, velocity and pressure fields behave respectively as

$$\mathbf{T}^s \sim r^{-\frac{1}{2}}, \quad \mathbf{v} \sim r^{\frac{1}{2}} \quad \text{and} \quad p \sim r^{-\frac{1}{2}}, \tag{4.52}$$

while for the polymer stress it is expected that

$$\mathbf{T} \sim \begin{cases} r^{-\frac{4}{11}}, & \text{PTT}, \\ r^{-\frac{5}{16}}, & \text{Giesekus}, \end{cases} \tag{4.53}$$

where r is the radial distance from the singularity. In particular, for the NS variables, the asymptotic results can be summarized as follows

$$\lambda \sim \begin{cases} r^{-\frac{15}{11}}, & \text{PTT}, \\ r^{-\frac{21}{16}}, & \text{Giesekus}, \end{cases} \quad \mu \sim \begin{cases} r^{-\frac{3}{22}}, & \text{PTT}, \\ r^{0}, & \text{Giesekus}, \end{cases} \quad \nu \sim \begin{cases} r^{\frac{12}{11}}, & \text{PTT}, \\ r^{\frac{21}{16}}, & \text{Giesekus}. \end{cases} \tag{4.54}$$

The asymptotic results predict that the solvent stress should dominate the polymer stress close to the singularity, which suggest that the kinematics are Newtonian-like. The above behaviours are expected to hold uniformly in angle, apart from near the stick and slip surfaces, where very thin cusp-like boundary layers are present.

We analyse the numerical results at the stick-slip transition point along the rays $\theta = \pi/2$ in Figures 9–10 and $\theta = 3\pi/4$ in Figures 11–12, these angles being illustrated in Fig. 8. Figure 9 presents the verification of the singularity behaviour for the velocity components and the pressure, whilst Fig. 10a),b) describes results for the polymer Cartesian extra-stress components. Also included are results for the NS variables in Fig. 10c),d). According to Fig. 9, we can confirm that the CSF and NSF produce similar results capturing the expected asymptotic behaviours for the velocity and pressure fields. However, for the components of extra-stress tensor depicted in Figs. 10a),b), it is evident that meshes M1 and M2 in both formulations are too coarse to capture the required behaviour for both fluid models. In particular, CSF struggles with the T_{22} component, which clearly needs a finer mesh and appears to converge slower to its asymptotics than the other two components. In contrast to the CSF, as illustrated in Figs. 10c),d), the NSF produces results in very good agreement with (4.54) capturing accurately the theoretical behaviours. Therefore, both formulations capture the required behaviours on meshes M2 and M3, but with clear differences in rate of convergence for the different components. Noteworthy, is the ability of the NSF to capture the NS behaviours even on the coarsest mesh M1. Similar behaviours are observed at $\theta = 3\pi/4$ as shown in Figs. 11–12. These results emphasize that smaller length scales are needed for the Cartesian stresses to capture

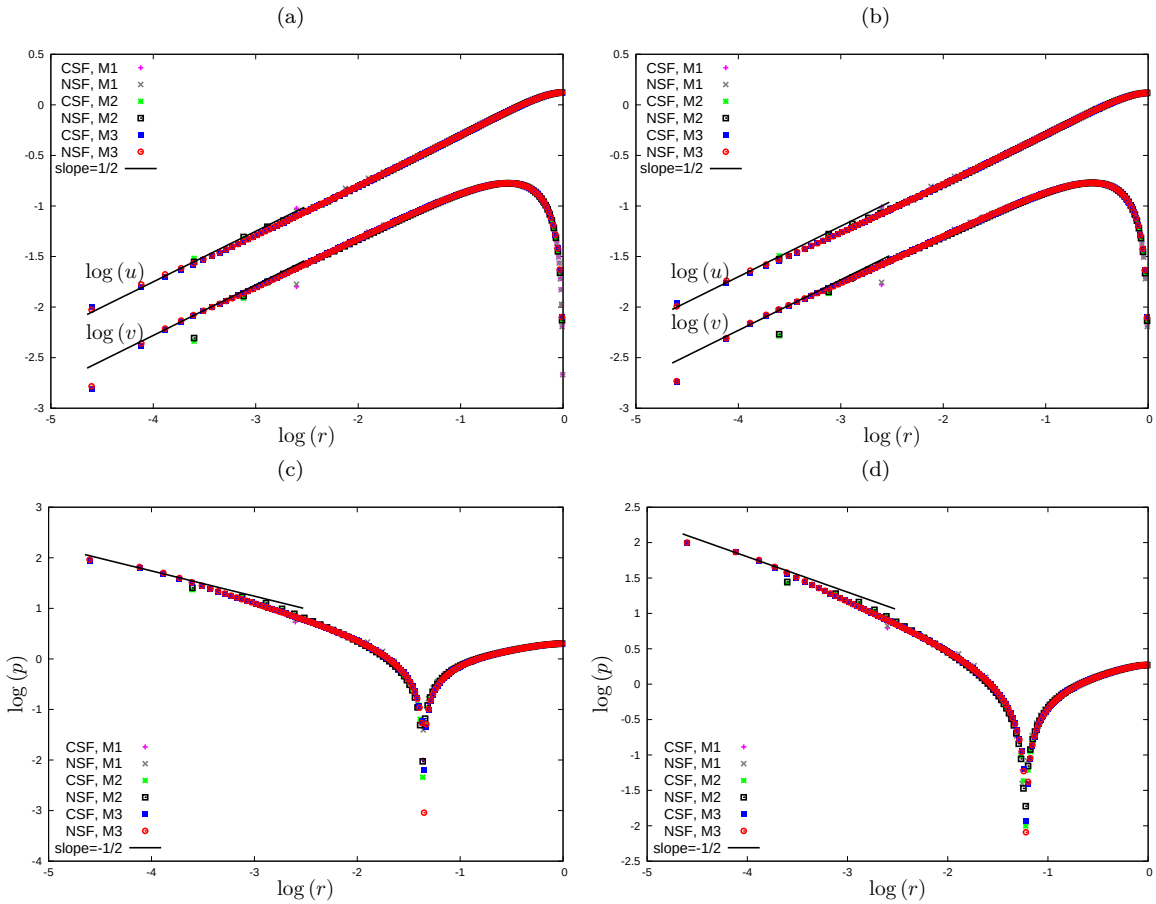

Figure 9: Asymptotic variation near the stick-slip transition point of (a) u, v (PTT), (b) u, v (Giesekus), (c) p (PTT) and (d) p (Giesekus) along the line $\theta = \pi/2$ with $\beta = 1/2$ and $Wi = 1$.

the singular behaviour compared to the natural stress variables. We also remark, that Cartesian extra-stress values calculated using the NS variables through (2.25)–(2.27) do not show a markedly significant improvement, in contrast to the re-entrant corner singularity (see in [34]).

The asymptotic solutions local to the singularity determined in [30,31] and [29] for the stream function (adjusted here for the current flow orientation) and natural stress variables are

$$\psi \sim 2C_0 r^{\frac{3}{2}} \sin\theta \cos\frac{\theta}{2}, \qquad \lambda \sim \frac{C_1}{C_0^2}\left(\frac{\psi}{C_0}\right)^{n_1}, \qquad \mu \sim C_2\left(\frac{\psi}{C_0}\right)^{n_2}, \qquad \nu \sim C_0^2 C_3\left(\frac{\psi}{C_0}\right)^{n_3}, \tag{4.55}$$

where

$$\begin{aligned} &\text{PTT:} && n_1 = -\frac{10}{11}, n_2 = -\frac{1}{11}, n_3 = \frac{8}{11}, \\ &\text{Giesekus:} && n_1 = -\frac{7}{8}, n_2 = 0, n_3 = \frac{7}{8}. \end{aligned} \tag{4.56}$$

Fitting these expressions to the NSF numerical solution, we may determine the four constants (C_0, C_1, C_2, C_3), estimates (from the ray $\theta = \pi/2$) being recorded in Table 2. For comparison, we also record the C_0 value in the Newtonian case, which agrees accurately with the analytical value reported in [6] of $(3/2\pi)^{1/2} \approx 0.691$. It is worth remarking that the numerical estimates for the constants along the ray $\theta = 3\pi/4$ give very similar values (agreeing to 1 d.p.) to those for $\theta = \pi/2$.

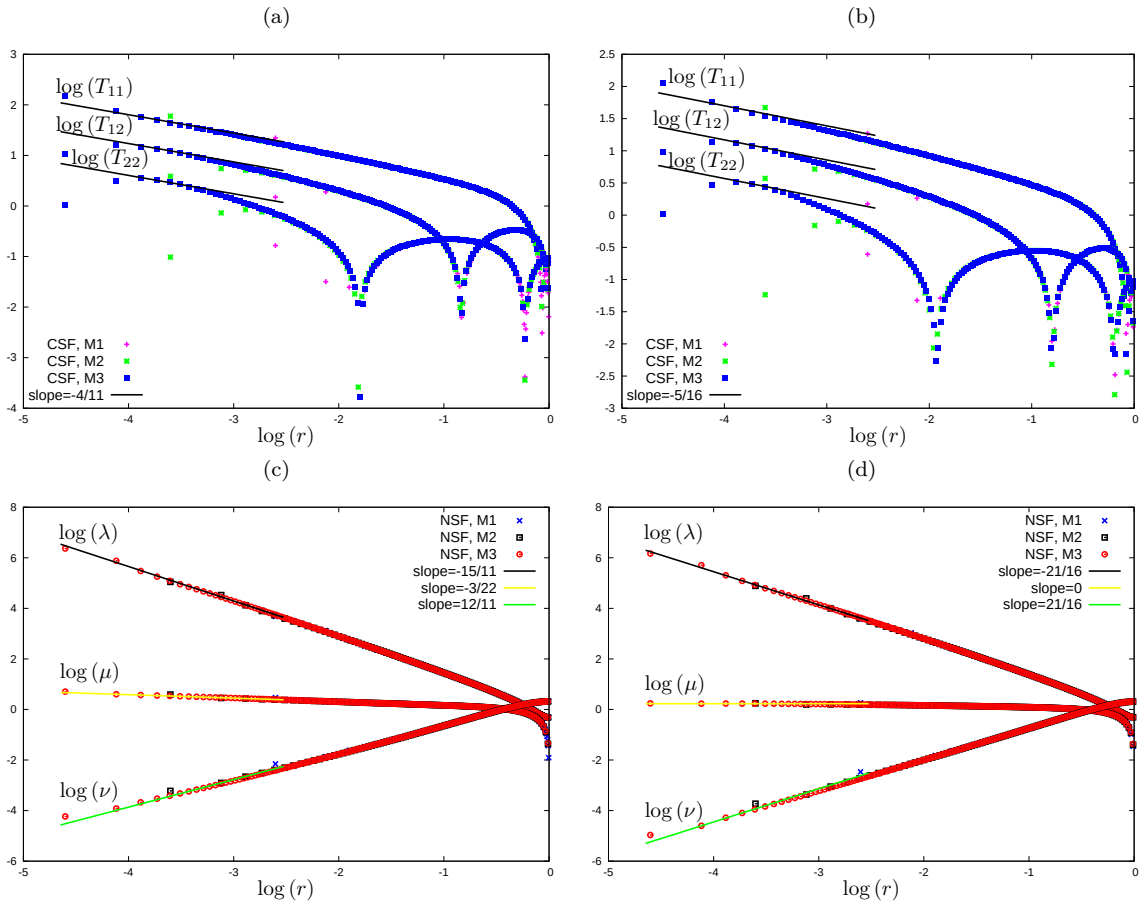

Figure 10: Asymptotic variation near the stick-slip transition point of (a) T_{11}, T_{12}, T_{22} (PTT), (b) T_{11}, T_{12}, T_{22} (Giesekus), (c) λ, μ, ν (PTT) and (d) λ, μ, ν (Giesekus) along the line $\theta = \pi/2$ with $\beta = 1/2$ and $Wi = 1$.

We now use these results to obtain estimates of the radial length scales on which the leading order Cartesian stress behaviours are expected to hold. The asymptotic behaviours (4.55) are predicated on the dominance of the solvent extra-stress $\mathbf{T}^s = 2\beta\mathbf{D}$ over the polymer extra-stress $\mathbf{T}$ i.e.

$$\mathbf{T} \ll \mathbf{T}^s \tag{4.57}$$

near the transition point, which should hold for non-zero β. Using the results in [29–31] we have that the polymer stress behaves as

$$\mathbf{T} \sim \frac{(1-\beta)}{Wi}\lambda \mathbf{v}\mathbf{v}^T \qquad \text{as } r \to 0, \tag{4.58}$$

where λ is recorded in (4.55). Since we are using local polar coordinates $x = r\cos\theta, y + 1 = r\sin\theta$ the stream function in (4.55) can be written as

$$\psi = \sqrt{2}C_0(y+1)\left((x^2 + (y+1)^2)^{\frac{1}{2}} + x\right)^{\frac{1}{2}}.$$

We can thus obtain expressions for the Cartesian velocity components and hence the solvent and polymer stresses, which are most conveniently written in polar coordinates as follows

$$u = C_0 r^{\frac{1}{2}} \cos\left(\frac{\theta}{2}\right)(3 - \cos\theta), \qquad v = -C_0 r^{\frac{1}{2}} \cos\left(\frac{\theta}{2}\right)\sin\theta,$$

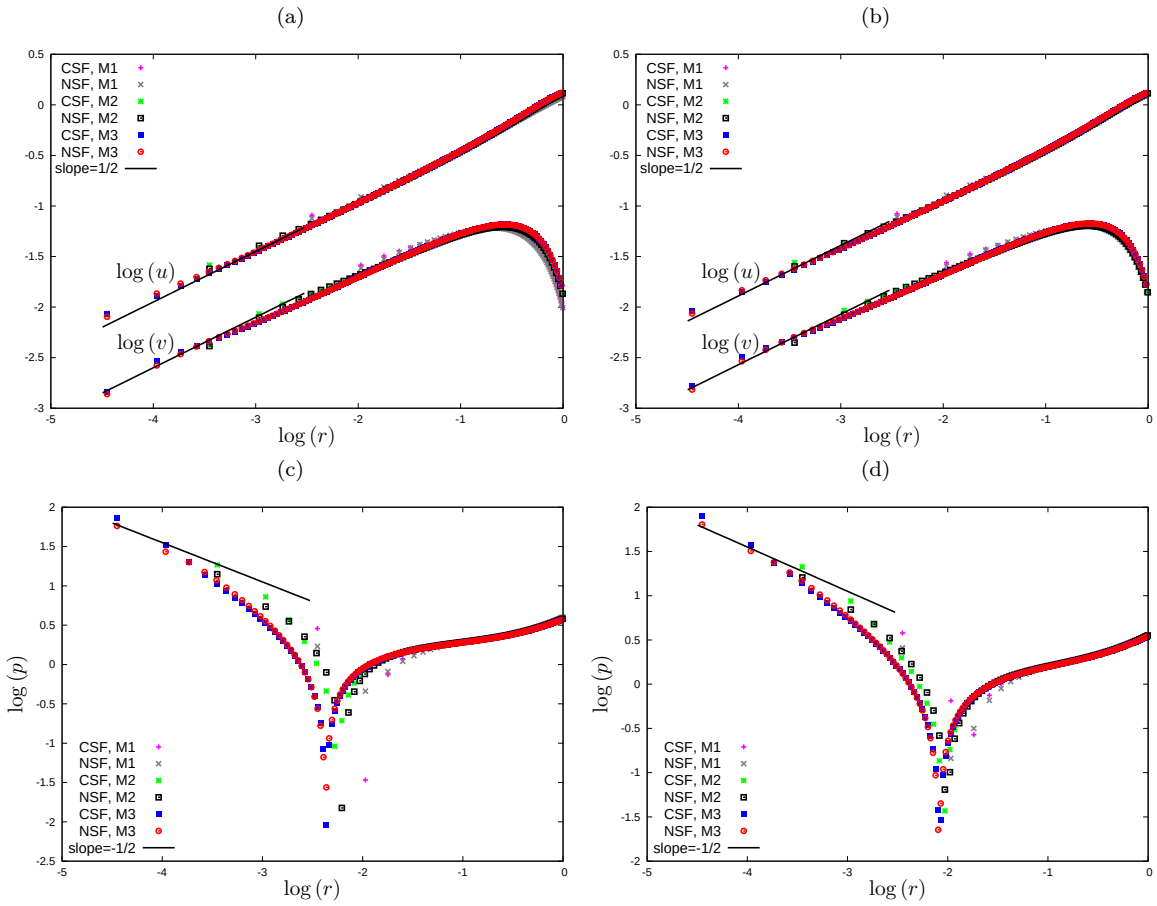

Figure 11: Asymptotic variation near the stick-slip transition point of (a) u, v (PTT), (b) u, v (Giesekus) (c) p (PTT) and (d) p (Giesekus) along the line $\theta = 3\pi/4$ with $\beta = 1/2$ and $Wi = 1$.

$$T^s_{ij} = \beta C_0 r^{-\frac{1}{2}} f_{ij}(\theta), \qquad T_{ij} = \frac{(1-\beta)}{Wi} C_1 r^{1+\frac{3}{2}n_1} h_{ij}(\theta),$$

where

$$f_{11}(\theta) = \cos\left(\frac{\theta}{2}\right)(2\cos^2\theta - \cos\theta + 1), \quad f_{12}(\theta) = \sin\left(\frac{\theta}{2}\right)(2\cos^2\theta + \cos\theta + 1), \quad f_{22}(\theta) = -f_{11}(\theta) \tag{4.59}$$

and

$$h_{11}(\theta) = \left(2\sin\theta\cos\left(\frac{\theta}{2}\right)\right)^{n_1}\cos^2\left(\frac{\theta}{2}\right)(3-\cos\theta)^2, \quad h_{12}(\theta) = h_{11}(\theta)\frac{\sin\theta}{(3-\cos\theta)}, \quad h_{22}(\theta) = h_{12}(\theta)\frac{\sin\theta}{(3-\cos\theta)} \tag{4.60}$$

with n_1 specified in (4.56). We may compare the absolute value of corresponding solvent and polymer components to obtain the radial estimates

$$r_{ij} = \left|\frac{\beta Wi}{(1-\beta)}\frac{C_0}{C_1}\frac{f_{ij}(\theta)}{h_{ij}(\theta)}\right|^{\frac{2}{3(n_1+1)}}. \tag{4.61}$$

The functions $|f_{ij}(\theta)/h_{ij}(\theta)|$ are plotted in Figure 13 and for uniform dominance of the solvent stress across the main interval of θ as illustrated by dotted lines in Figure 13, we require for the PTT and

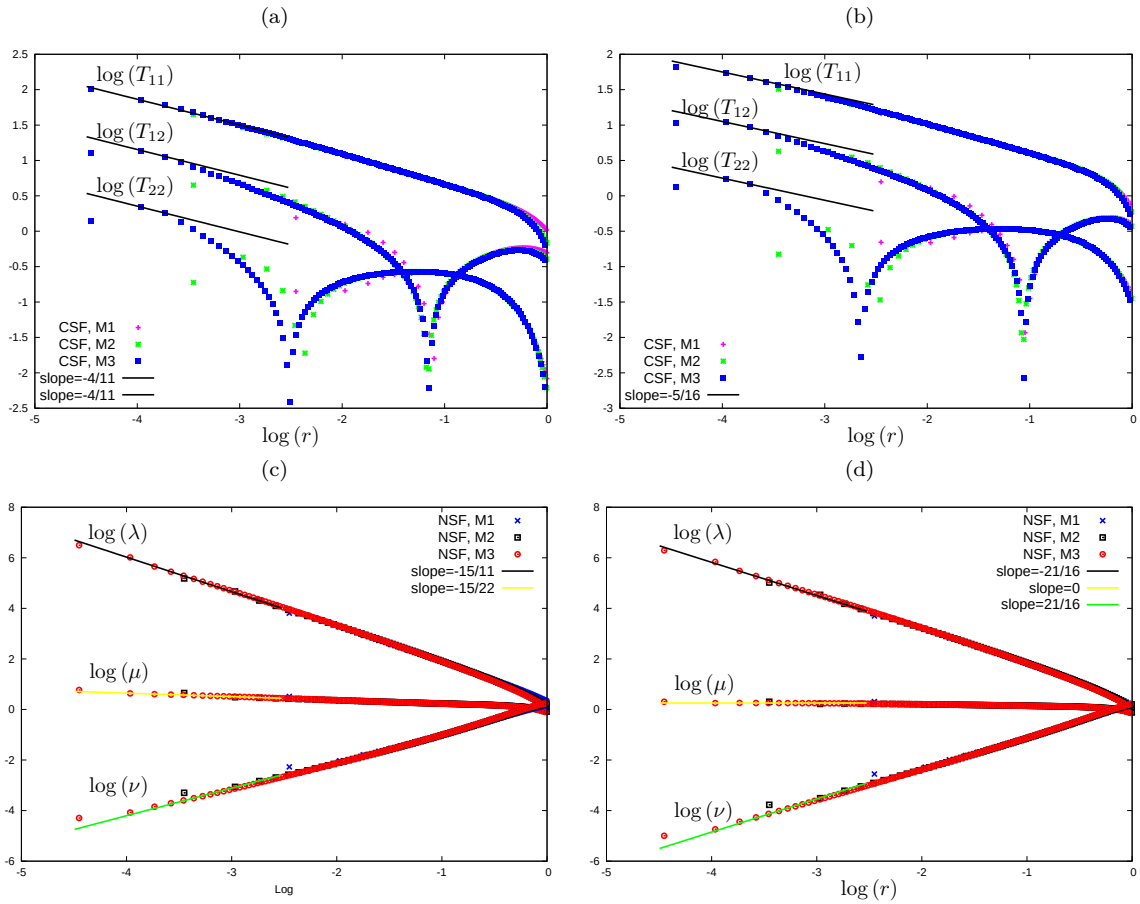

Figure 12: Asymptotic variation near the stick-slip transition point of (a) T_{11}, T_{12}, T_{22} (PTT), (b) T_{11}, T_{12}, T_{22} (Giesekus), (c) λ, μ, ν (PTT) and (d) λ, μ, ν (Giesekus) along the line $\theta = 3\pi/4$ with $\beta = 1/2$ and $Wi = 1$.

Giesekus models to use

$$\left|\frac{f_{11}}{h_{11}}\right| = 0.21, \qquad \left|\frac{f_{12}}{h_{12}}\right| = \begin{cases} 0.64, & \text{PTT}, \\ 0.63, & \text{Giesekus}, \end{cases} \qquad \left|\frac{f_{22}}{h_{22}}\right| = \begin{cases} 1.73, & \text{PTT}, \\ 1.71, & \text{Giesekus}, \end{cases} \tag{4.62}$$

which give the radial estimates recorded in the last three columns of Table 2 on using the estimates of the ratio C_0/C_1. It is clear that the radial estimates from the 11 and 12 components show that substantially smaller meshes are needed before their solvent stress components dominate those of the polymer.

4.2 Numerical investigation of the boundary layers

Additional insights on the stick-slip stress singularity behaviour may be gained by exploring the boundary layer structures. Here we compare the absolute magnitude of the terms in the CSF of the constitutive equations. We thus record

$$\max\left(\frac{|\mathbf{T}_{ij}|}{Wi}, |\overset{\triangledown}{\mathbf{T}}_{ij}|, \frac{\kappa}{(1-\beta)}|\mathbf{g}_{ij}|, \frac{2(1-\beta)}{Wi}|\mathbf{D}_{ij}|\right), \tag{4.63}$$

for each of the three components $ij = 11, 12$ and $= 22$ separately in Fig. 14. In these figures, we have considered a specific region nearby the singularity and the maps are labeled without the presence of the

Table 2: Estimate values of C_0, C_1, C_2 and C_3 as well as radial distances (4.61) for PTT and Giesekus models with $Wi = 1, \kappa = 0.1$ and fractional viscosity cases $\beta = 1/2$ and $\beta = 1/9$.

Model	C_0	C_1	C_2	C_3	r_{11}	r_{12}	r_{22}
Newtonian	0.692	–	–	–	–	–	–
				$\beta = 1/2$			
PTT	0.745	1.18	1.17	3.86	9×10^{-7}	3×10^{-3}	4.8
Giesekus	0.780	1.30	1.53	5.45	4×10^{-5}	1×10^{-2}	2.8
				$\beta = 1/9$			
PTT	0.712	1.13	1.26	4.35	9×10^{-16}	3×10^{-12}	5×10^{-9}
Giesekus	0.817	1.30	1.62	5.83	7×10^{-13}	3×10^{-10}	6×10^{-8}

modulus sign for convenience. Equations (2.9)–(2.11) give the explicit representation of the terms. The figures indicate the dominance of the upper convective polymer stress derivative (blue representation) near the singularity but away from the stick and slip boundaries. According to the first row of Figure 14, it dominates uniformly. The sub-plots in the second and third rows of Fig. 14 indicate that the rate-of-strain terms (green representation) dominate at the stick surface with the demarcation with the upper convected derivative terms being cusp like near the singularity (transition point). This supports the presence of the stick surface boundary layer, where the rate-of-strain terms must be recovered for viscometric behaviour. Similarly at the slip surface, it can be seen in the second row of Fig. 14 the dominance of the quadratic stress terms, as predicted theoretically for the slip boundary layer. These structures are apparent for both models. In order to clarify the threshold used to determine which term is dominant, we have also plotted in Figs. 15 the results of the four terms of (4.63) in the horizontal line $y \approx 1.999925$ (near to the singularity). The results in the ordinate axis are constructed using the log-scale. The results in this section used the parameter values $\beta = 1/2$, $Wi = 1$ and $\kappa = 0.1$.

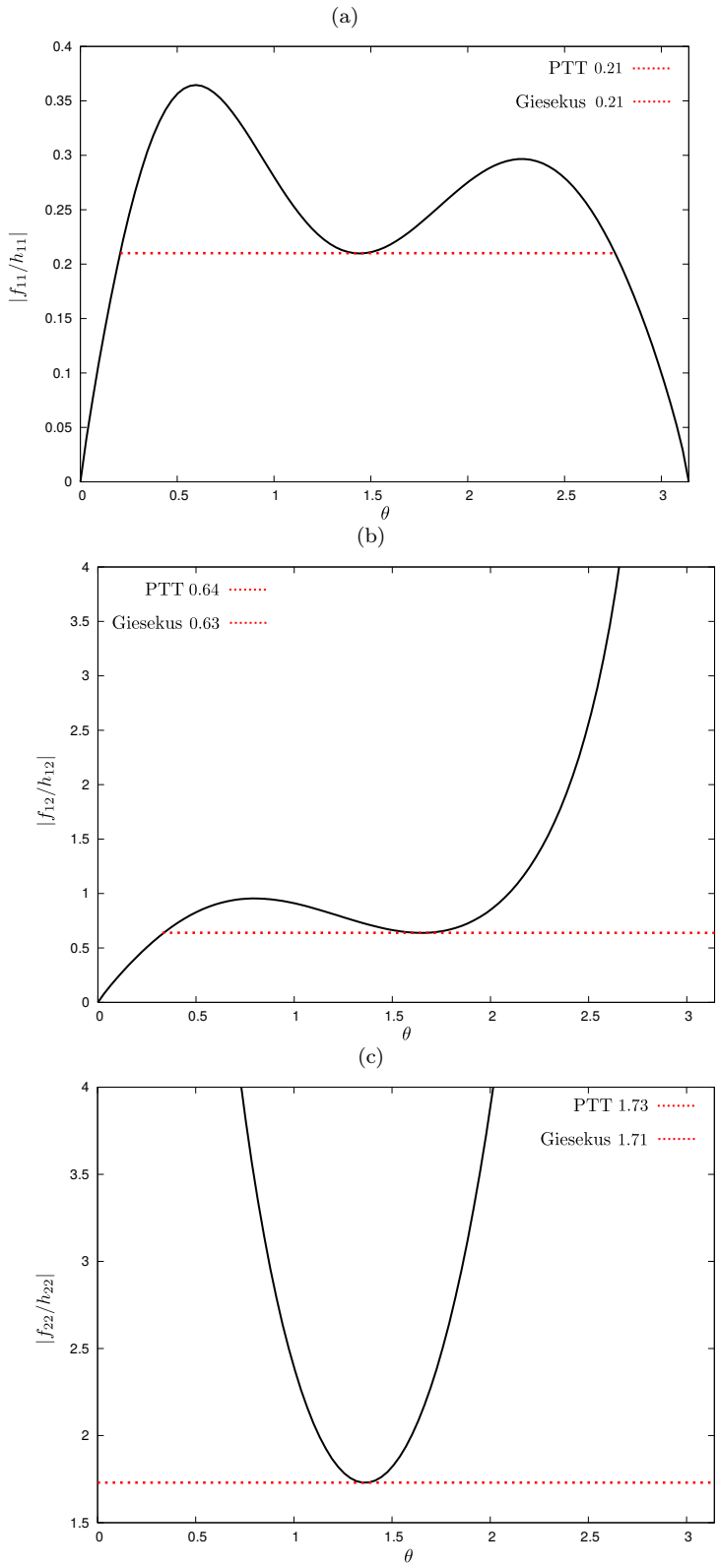

Figure 13: Variation of (a) $|f_{11}/h_{11}|$, (b) $|f_{12}/h_{12}|$ and (c) $|f_{22}/h_{22}|$ with θ for PTT $n_1 = -10/11$. The curves for Giesekus $n_1 = -7/8$ are almost identical.

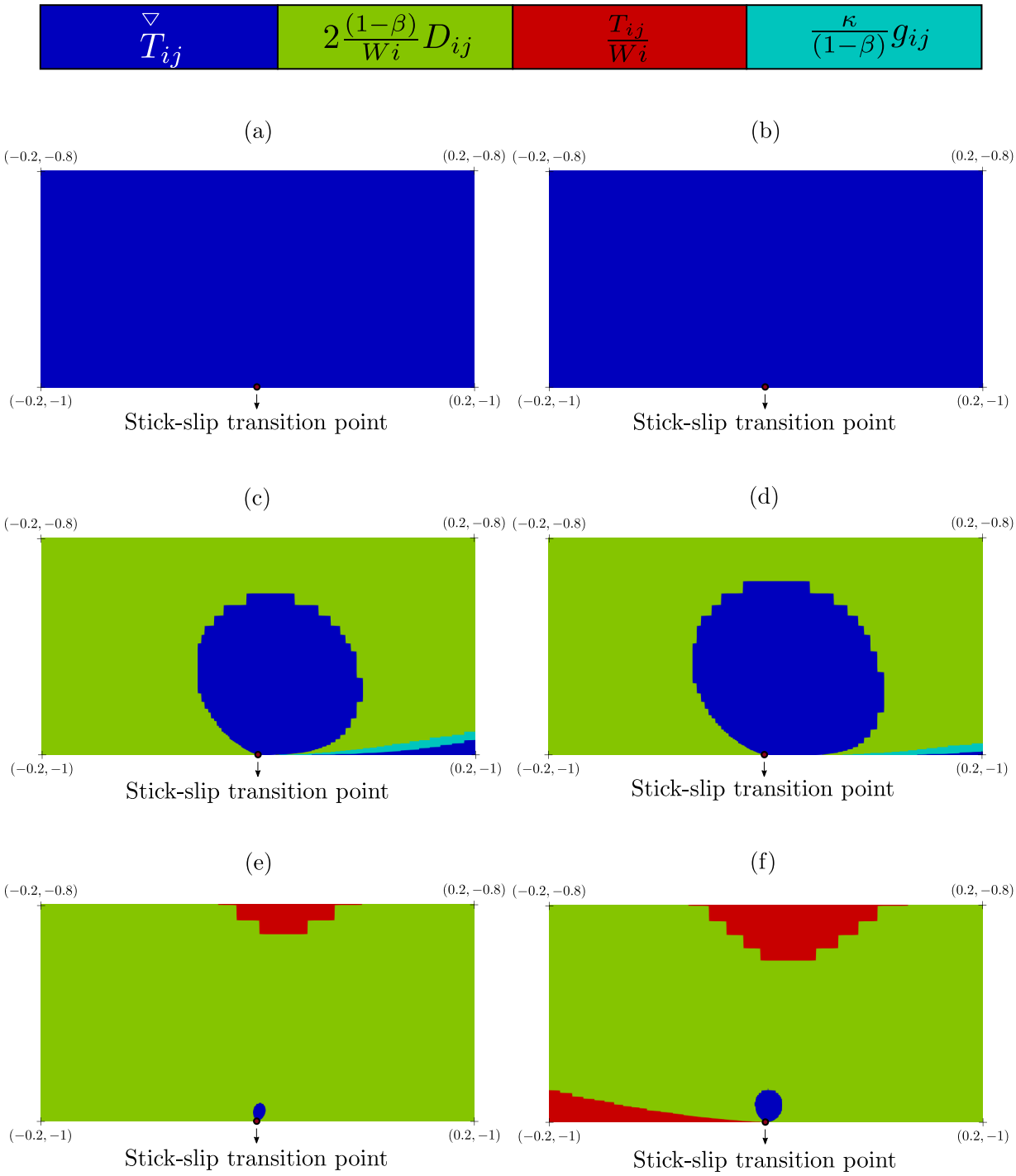

Figure 14: Dominance of the groups of terms (4.63) for components (a) $ij = 11$ (PTT), (b) $ij = 11$ (Giesekus), (c) $ij = 12$ (PTT), (d) $ij = 12$ (Giesekus), (e) $ij = 22$ (PTT) and (f) $ij = 22$ (Giesekus) within the Cartesian constitutive equation using $\beta = 1/2$ and $Wi = 1$.

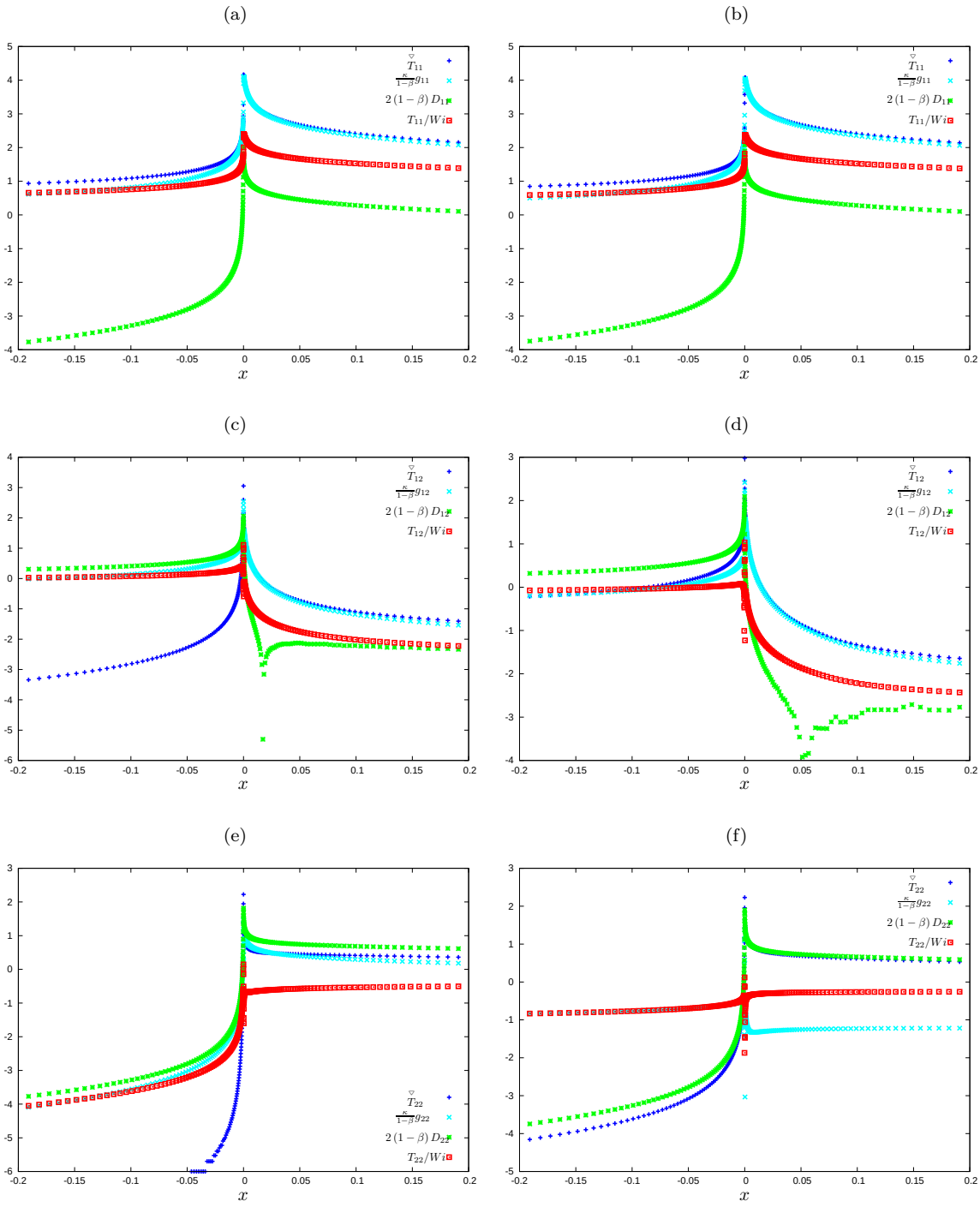

Figure 15: Dominance of the groups of terms (4.63) for components (a) $ij = 11$ (PTT), (b) $ij = 11$ (Giesekus), (c) $ij = 12$ (PTT), (d) $ij = 12$ (Giesekus), (e) $ij = 22$ (PTT) and (f) $ij = 22$ (Giesekus) within the Cartesian constitutive equation using $\beta = 1/2$ and $Wi = 1$.

4.3 Numerical investigation for small solvent viscosities

Here we examine the results for the smaller fractional viscosity ratio of $\beta = 1/9$. Due to the CFL stability restriction in the time-step, to achieve numerical results on our finest mesh M3, we are limited

spatially to considering a reduced domain, e.g., the dimensionless domain half-length is now taken as $L = 4$. Although the global results will not be accurate, it is worth noting that this truncated channel length will not change the numerical structure of the stress singularities near to the stick-slip transition point, including the estimates of the constants presented in Table 2. We base this statement on observing that the results for $\beta = 1/2$ in section 4.1 did not change when $L = 8$ was reduced to $L = 4$.

Figures 16–17 reproduce the results of previous Figures 9–10, but for the case $\beta = 1/9$. Whilst the velocity and extra-stresses (both Cartesian and Natural) illustrate convergence to the theoretical behaviours, the pressure does not, suggesting the need for a more refined mesh for this variable. However, the fall off in the Cartesian components T_{12} and T_{22} for the closest points is noteworthy for both models and reminiscent of behaviour at the re-entrant corner singularity in contraction flow (see, for example [48]). The radial distance estimates (4.61) have now reduced significantly for this fractional viscosity and are recorded in Table 2. This is mainly due to the effect of the power of β in the expressions, the power being $7\frac{1}{3}$ for PTT and $5\frac{1}{3}$ for Giesekus (the constants C_0, C_1 are relatively insensitive to changes in β). It also highlights the extreme challenge that numerical schemes face in capturing the singularity for small solvent viscosities (and in fact the emergence of another, as yet theoretically unknown singularity as the solvent viscosity vanishes in the limit $\beta \to 0$).

The plots for the velocities and extra-stresses confirm no significant variations in the predicted slopes from the theoretical ones, confirming the insensitivity of the power-law exponents in (4.55) to the solvent fraction. Results for $\beta = 1/9$ along the ray $\theta = \frac{3\pi}{4}$ are also presented in Figs. 18–19.

The Cartesian boundary layer plots in Figure 20, emphasise the shrinking dominance of the upper-convected stress derivative near to the singularity and hence the relevance of the stretching solution (4.58). For the PTT 22 component, it is no longer visible. Evidence of cusp-like boundary layers at both the stick and slip surfaces are still apparent in the 12 component plots. Additionally, we have also described in Figs. 21, the profiles of the four terms of (4.63) in the horizontal line $y \approx 1.999925$

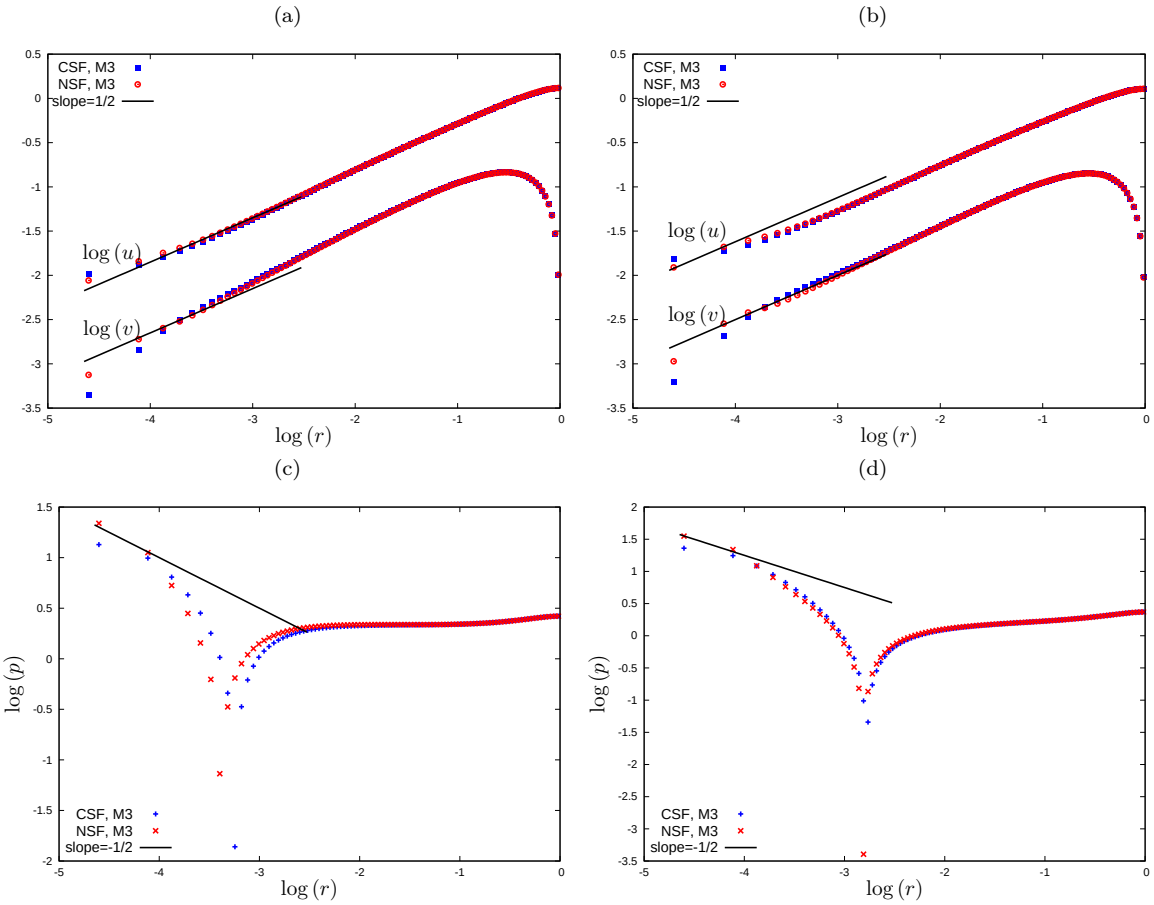

Figure 16: Asymptotic variation near the stick-slip transition point of (a) u, v (PTT), (b) u, v (Giesekus), (c) p (PTT) and (d) p (Giesekus) along the line $\theta = \pi/2$ considering the half-length $L = 4$ with $\beta = 1/9$.

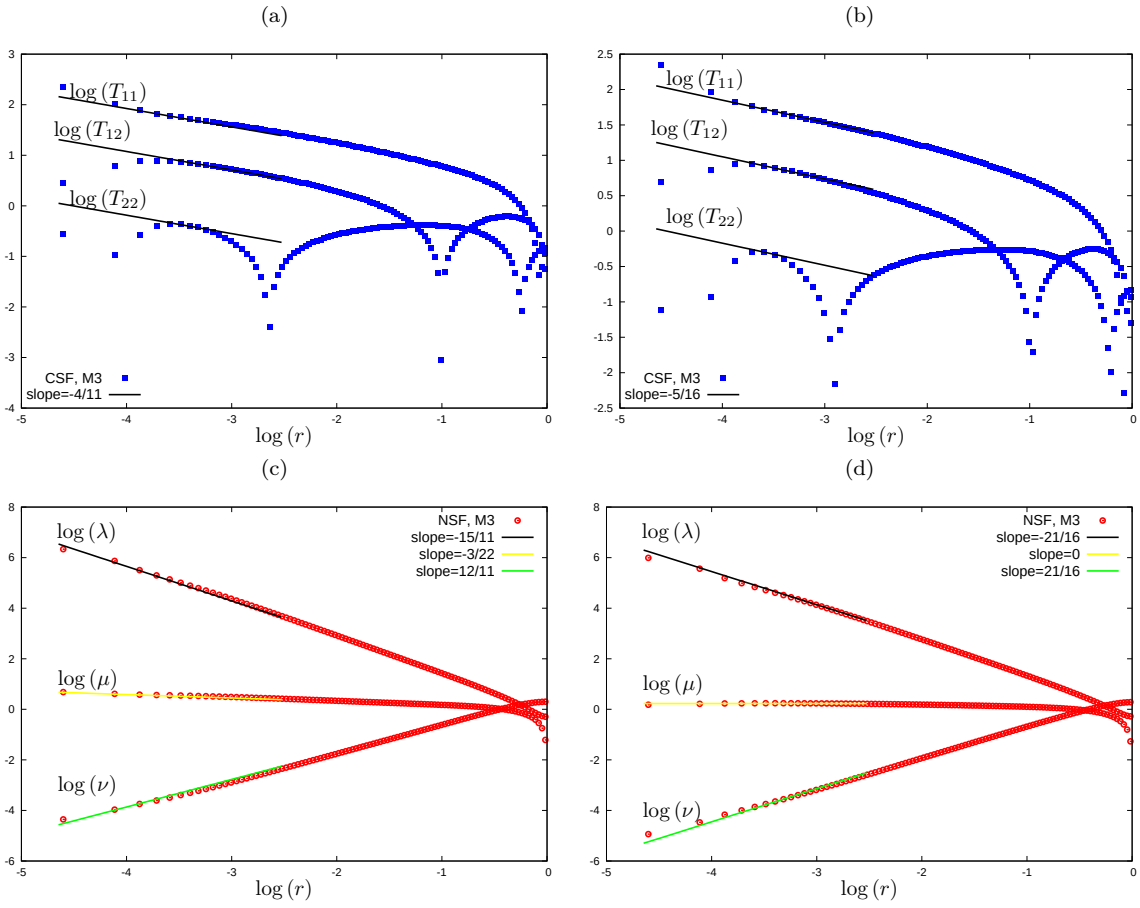

Figure 17: Asymptotic variation near the stick-slip transition point of (a) T_{11}, T_{12}, T_{22} (PTT), (b) T_{11}, T_{12}, T_{22} (Giesekus), (c) λ, μ, ν (PTT) and (d) λ, μ, ν (Giesekus) along the line $\theta = \pi/2$ considering the half-length $L = 4$ with $\beta = 1/9$.

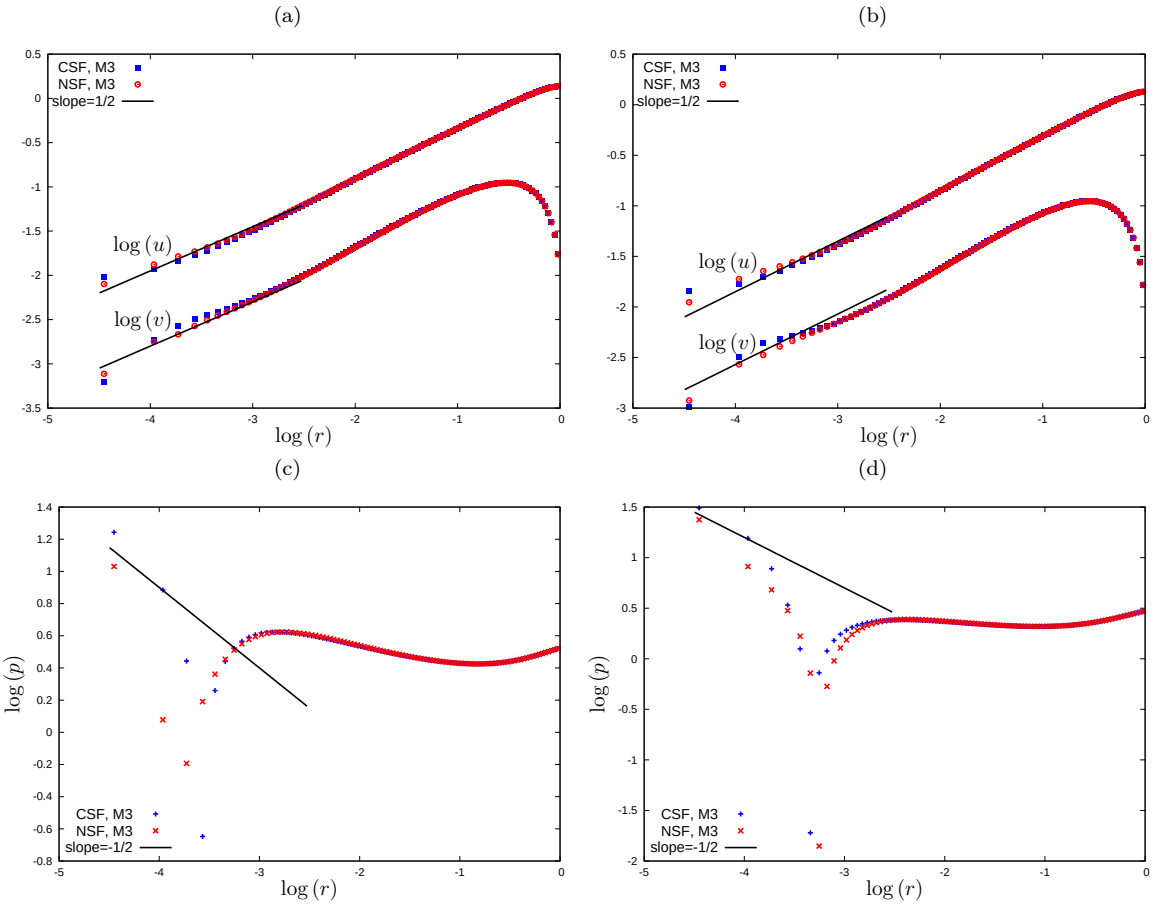

Figure 18: Asymptotic variation near the stick-slip transition point of (a) u, v (PTT), (b) u, v (Giesekus), (c) p (PTT) and (d) p (Giesekus) along the line $\theta = 3\pi/4$ considering the half-length $L = 4$ with $\beta = 1/9$.

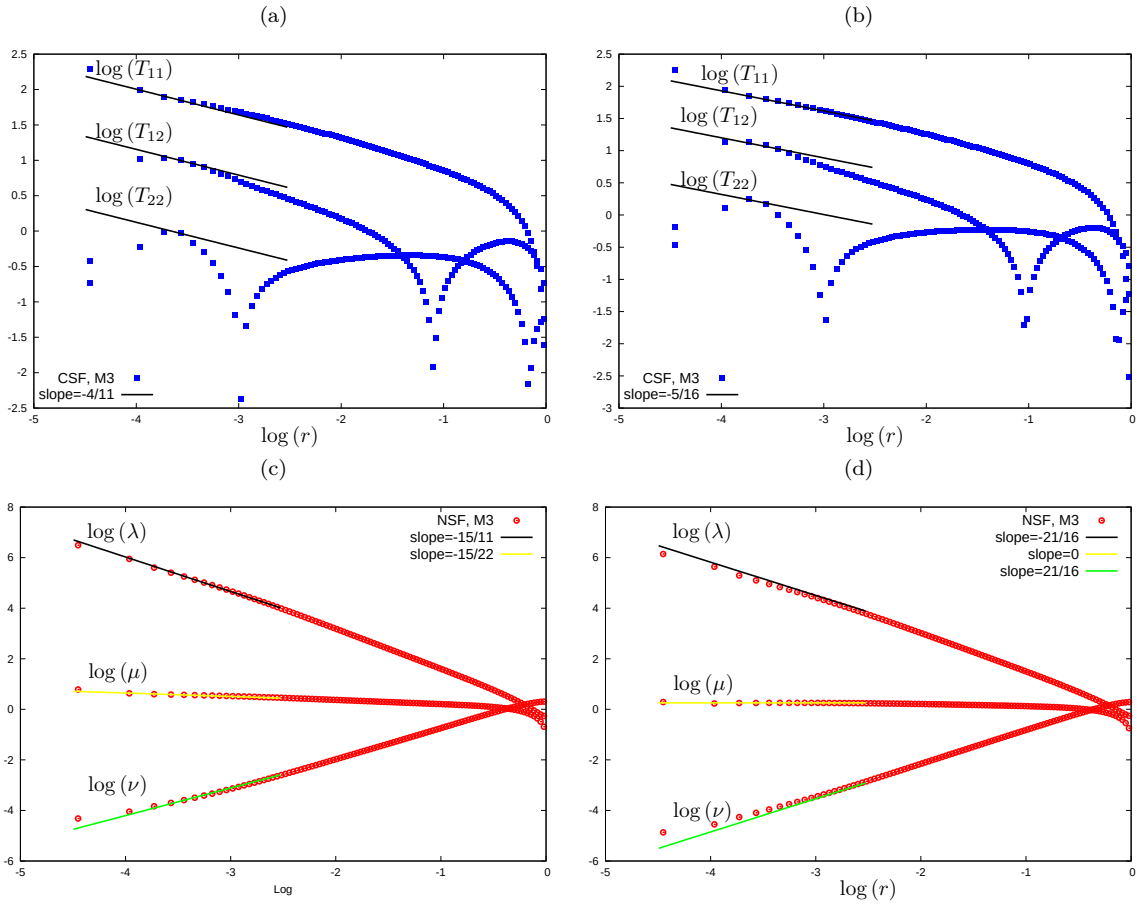

Figure 19: Asymptotic variation near the stick-slip transition point of (a) T_{11}, T_{12}, T_{22} (PTT), (b) T_{11}, T_{12}, T_{22} (Giesekus), (c) λ, μ, ν (PTT) and (d) λ, μ, ν (Giesekus) along the line $\theta = 3\pi/4$ considering the half-length $L = 4$ with $\beta = 1/9$.

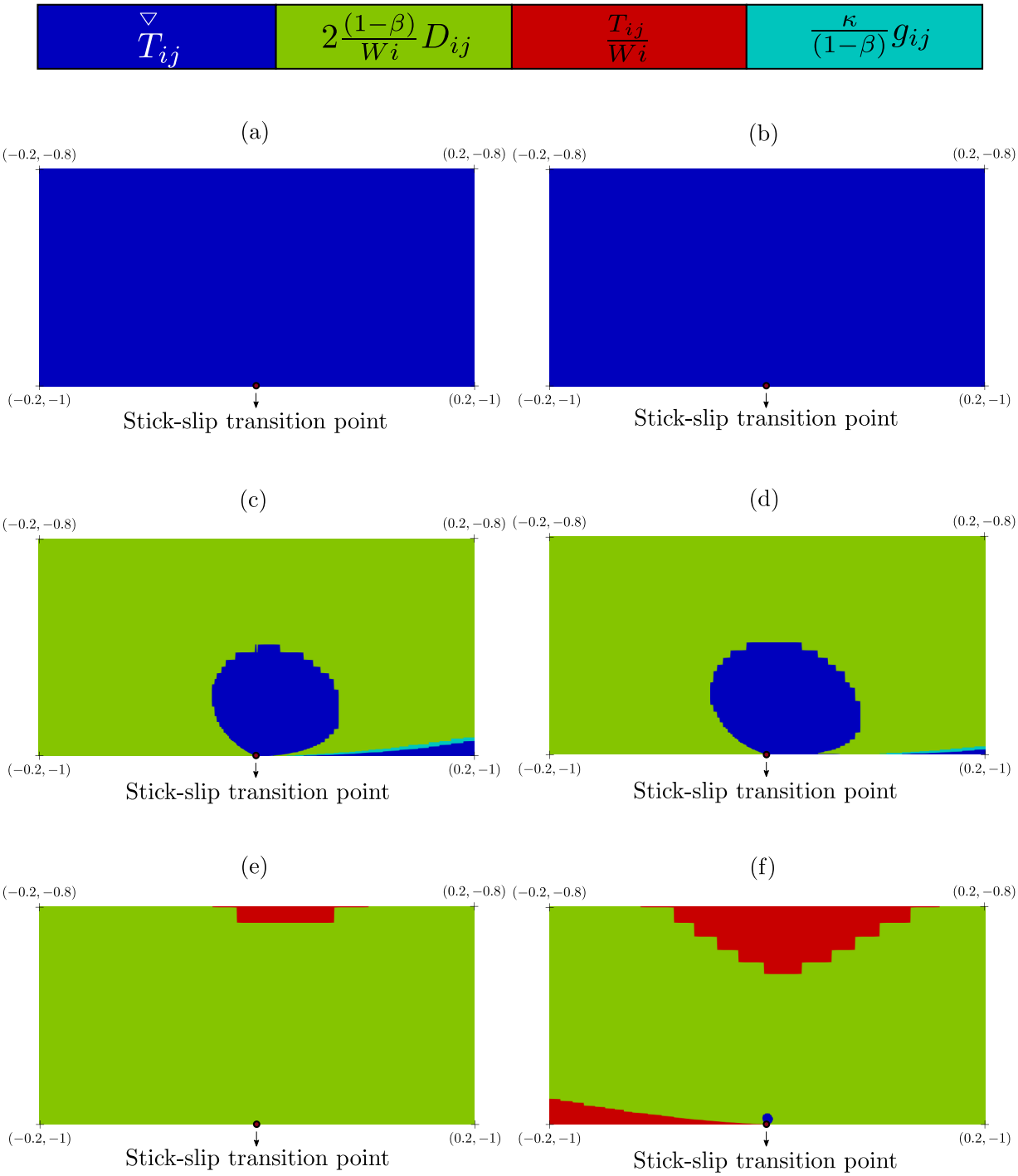

Figure 20: Dominance of the groups of terms (4.63) for the components (a) $ij = 11$ (PTT), (b) $ij = 11$ (Giesekus), (c) $ij = 12$ (PTT), (d) $ij = 12$ (Giesekus), (e) $ij = 22$ (PTT) and (f) $ij = 22$ (Giesekus) within the Cartesian constitutive equation using $\beta = 1/9$ and $Wi = 1$.

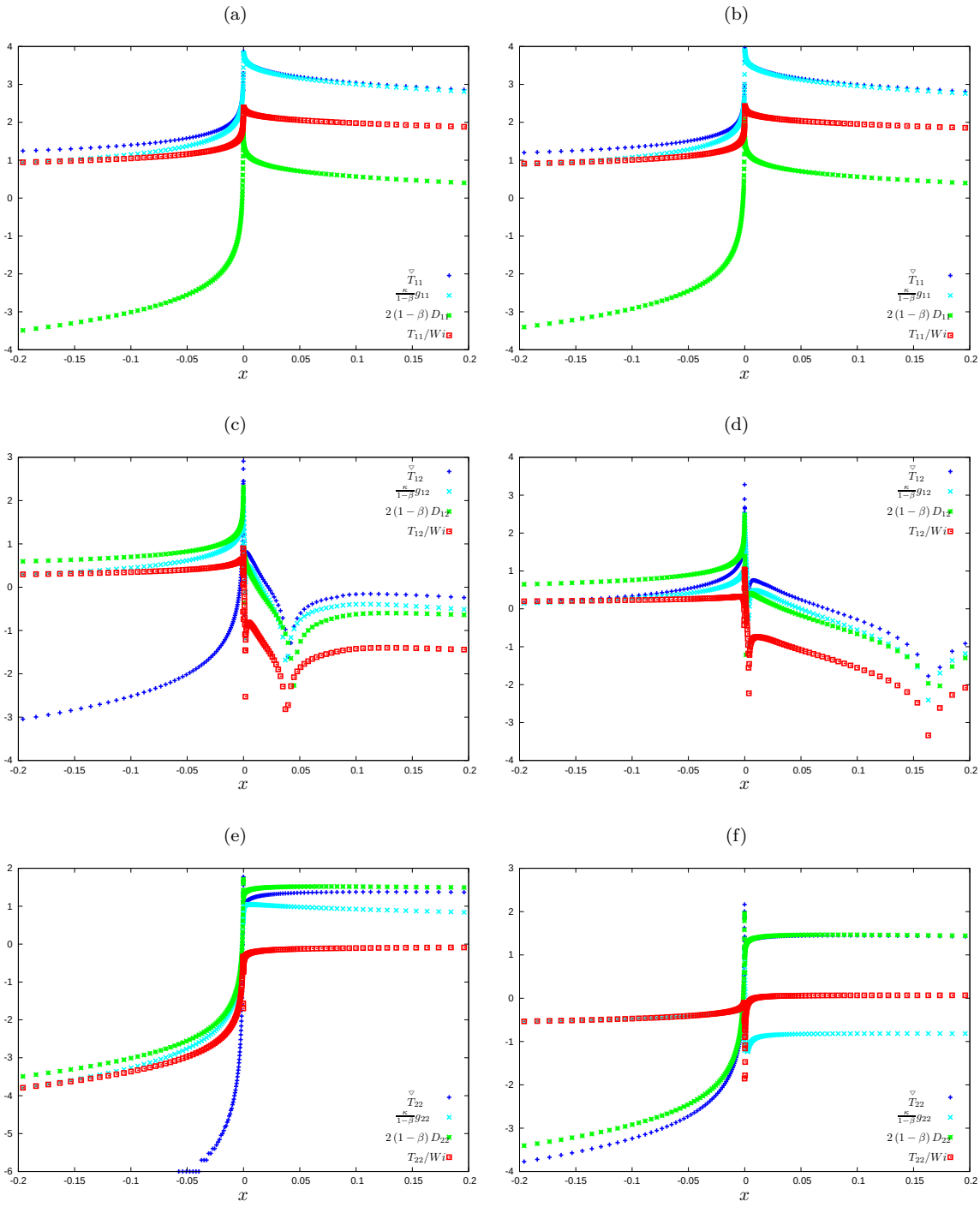

Figure 21: Dominance of the groups of terms (4.63) for the components (a) $ij = 11$ (PTT), (b) $ij = 11$ (Giesekus), (c) $ij = 12$ (PTT), (d) $ij = 12$ (Giesekus), (e) $ij = 22$ (PTT) and (f) $ij = 22$ (Giesekus) within the Cartesian constitutive equation using $\beta = 1/9$ and $Wi = 1$.

4.4 Influence of the Weissenberg number

In this section we numerically show that the stick-slip singularity is independent of the Weissenberg number, varying this number as 5, 10 and 15. In order to save CPU time and maintain numerical stability,

Table 3: Estimate values of C_0, C_1, C_2 and C_3 as well as radial distances (4.61) for PTT model with $\kappa = 0.1$ and fractional viscosity $\beta = 1/2$.

Wi	C_0	C_1	C_2	C_3	r_{11}	r_{12}	r_{22}
1	0.748	1.19	1.18	3.86	3.53×10^{-7}	1.23×10^{-3}	1.84
5	0.775	4.70	2.07	3.18	2.58×10^{-6}	9.04×10^{-3}	1.34
10	0.783	8.15	2.59	2.93	7.93×10^{-6}	2.77×10^{-2}	41.36
15	0.788	11.19	2.96	2.79	1.59×10^{-5}	5.56×10^{-2}	82.91

we use the intermediate mesh M2 (see Table 1) for the truncation length $L = 8$ and $\beta = 1/2$. We mention that the dimensionless domain half-length adopted in our study did not influence the numerical results captured in the vicinity of the singularity, as shown by the results in the Appendix B.

Figures 22 and 23 confirm that the leading order asymptotic behaviours of the variables are independent of the selected Weissenberg numbers. For the velocity and pressure behaviours in Fig. 22, the CSF and NSF produce very similar results. The extra-stress components of the CSF are shown in Fig. 23(a), whilst the natural stress variables are given in Fig. 23 (b). It is noteworthy that increasing Wi leads to improvement in the slope results for the T_{22} component in the CSF.

The influence of the Weissenberg number on the analytical constants (C_0, C_1, C_2, C_3) (see eq. 4.55) from the ray $\theta = \pi/2$ are described in Table 3. Results for the dominance of the terms for PTT with selected Wi are shown Fig. 24, with only the 12 and 22 components plotted, since there being no change for the 11 component to that seen in Fig. 14(a) for $Wi = 1$. The maps illustrate the growing dominance of the upper convected stress derivative term as the Weissenberg number is increased, with Table 3 showing increasing radial distances on which the singularity is anticipated to be found. A profile investigation is also presented in Fig. 25 to quantify the dominance of the terms on the boundary layer structures.

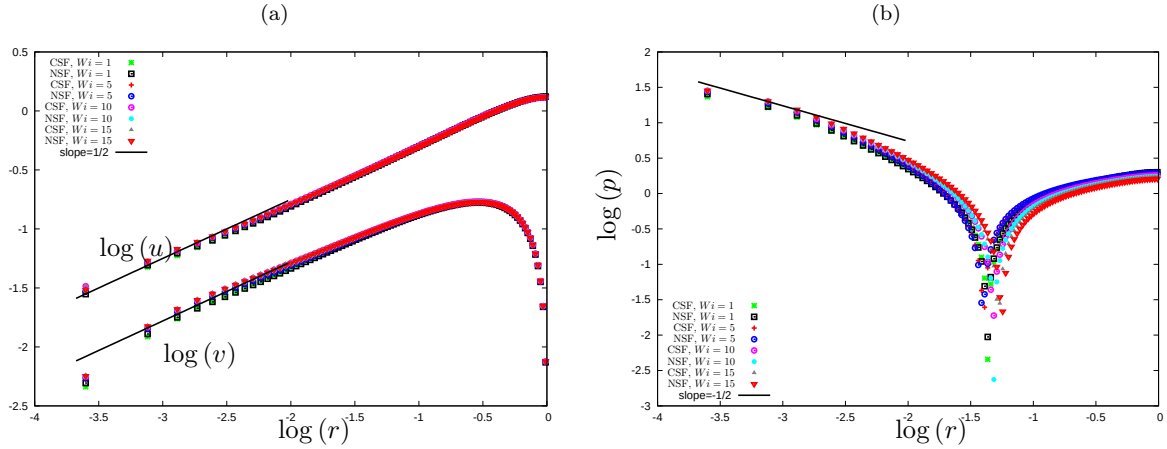

Figure 22: Asymptotic variation near the stick-slip transition point of (a) u, v and (b) p along the line $\theta = \pi/2$ for PTT with $\beta = 1/2$. The Weissenberg numbers adopted were $Wi = 1, 5, 10, 15$.

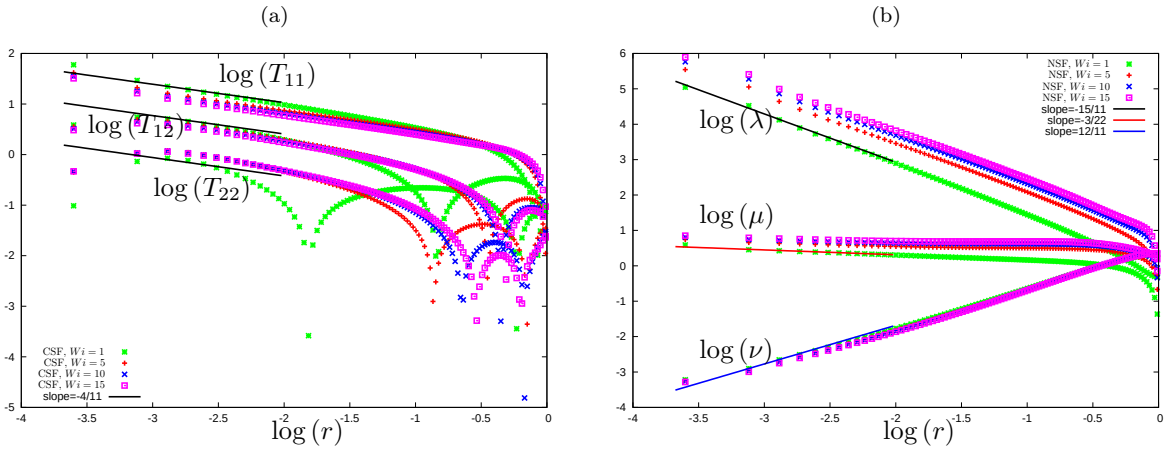

Figure 23: Asymptotic variation near the stick-slip transition point of (a) T_{11}, T_{12}, T_{22} and (b) λ, μ, ν along the line $\theta = \pi/2$ for PTT with $\beta = 1/2$. The Weissenberg numbers adopted were $Wi = 1, 5, 10, 15$.

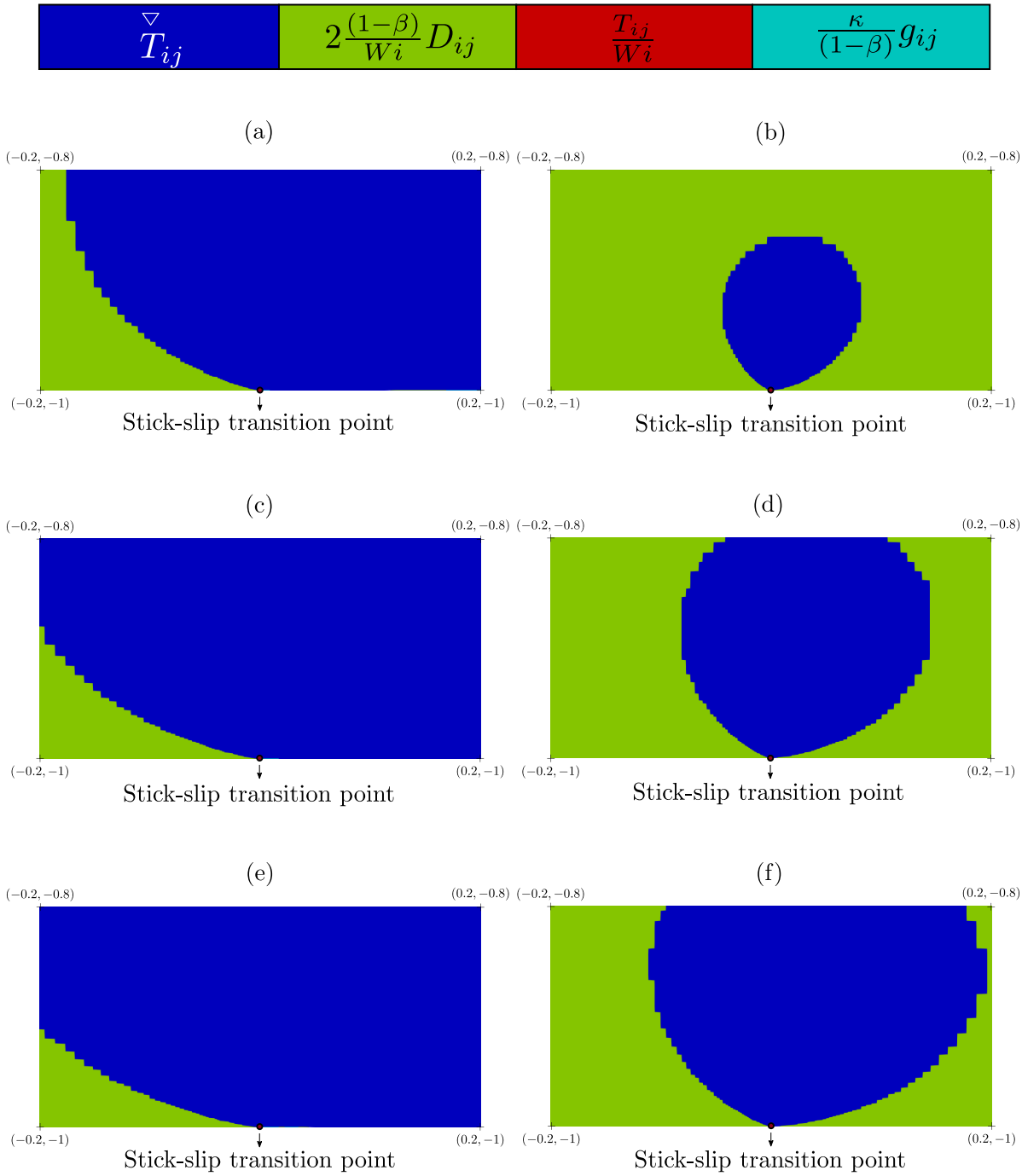

Figure 24: Dominance of the groups of terms (4.63) for components 12 and 22 within the Cartesian constitutive equation for PTT with $\beta = 1/2$: first row for $Wi = 5$ and components (a) $ij = 12$, (b) $ij = 22$, second row for $Wi = 10$ and components (c) $ij = 12$, (d) $ij = 22$ and third row for $Wi = 15$ and components (e) $ij = 12$, (f) $ij = 22$.

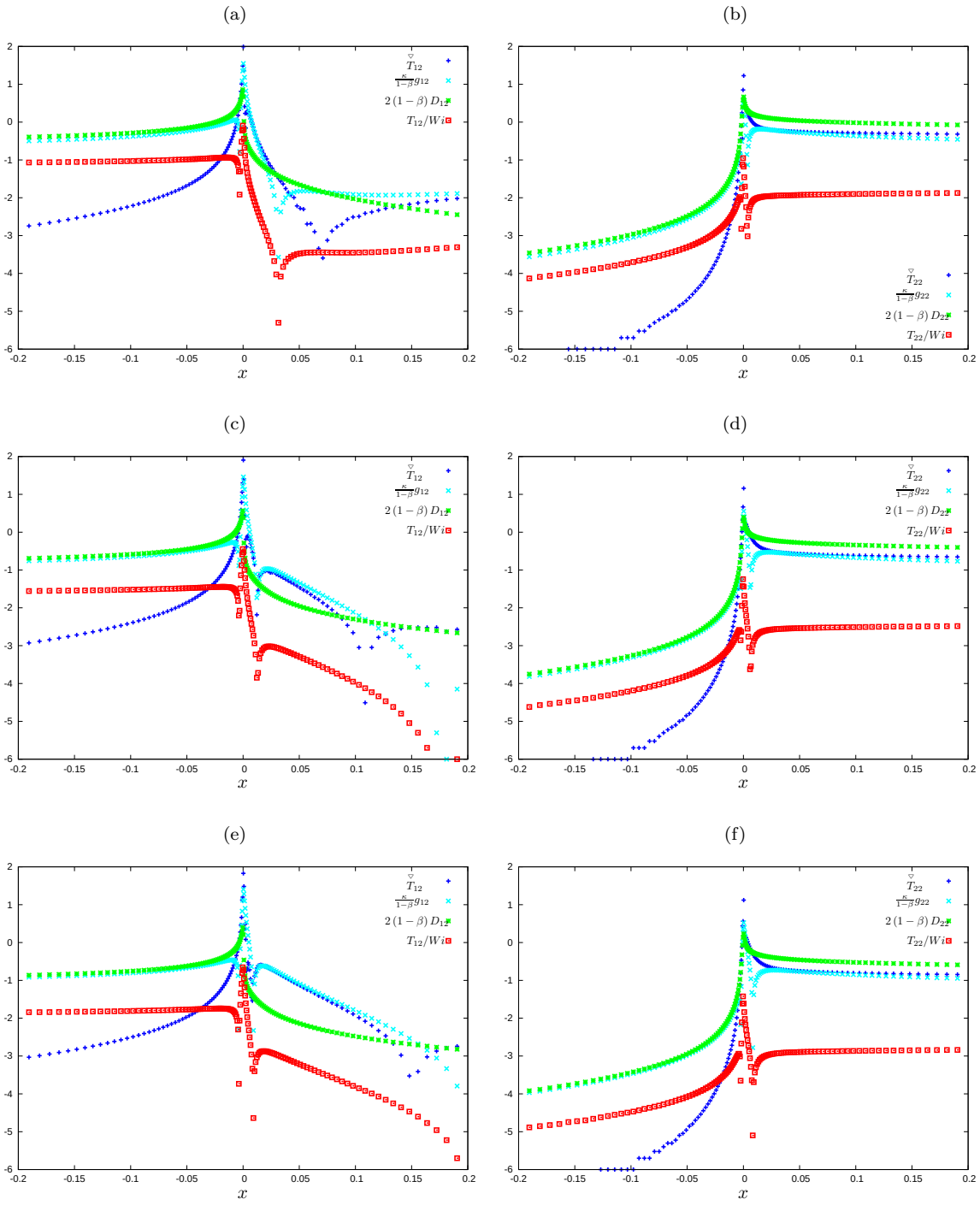

Figure 25: Dominance of the groups of terms (4.63) for components 12 and 22 within the Cartesian constitutive equation for PTT with $\beta = 1/2$: first row for $Wi = 5$ and components (a) $ij = 12$, (b) $ij = 22$, second row for $Wi = 10$ and components (c) $ij = 12$, (d) $ij = 22$ and third row for $Wi = 15$ and components (e) $ij = 12$, (f) $ij = 22$.

5 Discussion

A finite-difference numerical scheme using a semi-explicit projection method has been implemented to address the planar stick-slip flow for the PTT and Giesekus viscoelastic models. The scheme solves the transient problem and has been applied to two different formulations of the polymer constitutive equations, the traditional formulation using Cartesian stresses (CSF) and the other using natural stresses (NSF). The Cartesian stress formulation uses a fixed basis for the polymer stress, whilst the natural stress formulation aligns the polymer extra-stress along particle paths/streamlines.

The purpose of the investigation was to understand the efficacy of both formulations in a flow problem with a challenging singularity present. The main conclusion of the numerical tests in section 3, is the significant improvement in the rate of convergence both temporally for the extra-stress residuals and spatially in capturing the stress singularity behaviour that the NSF affords over the CSF. In addition, as presented in section 4, the NSF results allow consistent estimates of the constants in the asymptotic behaviours (4.55), which in turn can be used to derive theoretical estimates in Table 2 of the length scales on which the solvent stress dominates the polymer stress near to the singularity. For $\beta = 1/2$ these suggest radial distances of 10^{-6} for PTT and 10^{-5} for Giesekus, where the pressure and Cartesian T_{22} component are the slowest convergent variables and only just beginning to attain their singular behaviours on the finest mesh M3. The situation is starkly different for the smaller fractional viscosity case of $\beta = 1/9$. Whilst the natural stress variables capture their singular behaviours, the Cartesian components clearly struggle even on the finest mesh M3. The radial estimates in Table 2 have now reduced considerably, illustrating the severe challenge capturing the singularity possess to the Cartesian formulation for small solvent viscosity. It is on these radial distances that the theoretical asymptotic structure at the singularity presented in [30,31] is expected to be found. However, numerical evidence of the structure is still apparent on larger length scales, as evidenced in the dominance plots for each group of terms in the component equations of the Cartesian form of the polymer constitutive equations. As is often the case, and apparent here, the asymptotic results can hold on scales larger than their strict region of validity.

Acknowledgements

The authors would like to thank the financial support given by SPRINT/FAPESP grant no. 2018/22242-0. C.M. Oishi acknowledges CNPq (Conselho Nacional de Desenvolvimento Científico e Tecnologico), grant no. 307459/2016-0 and FAPESP (Fundação de Amparo à Pesquisa do Estado de São Paulo) grants no. 2013/07375-0. I. L. Palhares Junior acknowledges the financial support of FAPESP grants no. 2014/17348-2 and BEPE no. 2016/20389-8.

References

[1] J.R.A. Pearson. *Mechanics of Polymer Processing -application to Polymer Processing (videorecording)*. Center for Advanced Engineering Study, M.I.T., Cambridge, Mass., 1974.

[2] R.I. Tanner. *Engineering Rheology*. The Oxford engineering science series. Clarendon, 1985.

[3] S. Richardson. A stick-slip problem related to the motion of a free jet at low reynolds numbers. In *Mathematical Proceedings of the Cambridge Philosophical Society*, volume 67, pages 477–489. Cambridge University Press, 1970.

[4] S. Richardson. The die swell phenomenon. *Rheologica Acta*, 9(2):193–199, Apr 1970.

[5] S. A. Trogdon and D. D. Joseph. The stick-slip problem for a round jet. *Rheologica Acta*, 19(4):404–420, Jul 1980.

[6] R.I. Tanner and X. Huang. Stress singularities in non-newtonian stick-slip and edge flows. *Journal of Non-Newtonian Fluid Mechanics*, 50(2):135 – 160, 1993.

[7] T. R. Salamon, D. E. Bornside, R. C. Armstrong, and R. A. Brown. The role of surface tension in the dominant balance in the die swell singularity. *Physics of Fluids*, 7(10):2328–2344, 1995.

[8] Christopher J. S. Petrie and M. M. Denn. Instabilities in polymer processing. *AIChE Journal*, 22(2):209–236.

[9] M. M. Denn. Issues in viscoelastic fluid mechanics. *Annual Review of Fluid Mechanics*, 22(1):13–32, 1990.

[10] M. M. Denn. Extrusion instabilities and wall slip. *Annual Review of Fluid Mechanics*, 33(1):265–287, 2001.

[11] R. G. Larson. Instabilities in viscoelastic flows. *Rheologica Acta*, 31(3):213–263, May 1992.

[12] Michael D. Graham. The sharkskin instability of polymer melt flows. *Chaos: An Interdisciplinary Journal of Nonlinear Science*, 9(1):154–163, 1999.

[13] Youngdon Kwon. Numerical modelling of two-dimensional melt fracture instability in viscoelastic flow. *Journal of Fluid Mechanics*, 855:595–615, 2018.

[14] O. Hassager. Working group on numerical techniques. In *Proceedings of the Vth Workshop on Numerical Methods in Non-Newtonian Flow, J. Non-Newtonian Fluid Mech.*, volume 29, pages 2–5, 1988.

[15] M. Renardy. *Mathematical analysis of viscoelastic flows*. Society for Industrial and Applied Mathematics, SIAM, Philadelphia, 2000.

[16] Nhan Phan Thien and Roger I. Tanner. A new constitutive equation derived from network theory. *Journal of Non-Newtonian Fluid Mechanics*, 2(4):353 – 365, 1977.

[17] N. PhanâĂŘThien. A nonlinear network viscoelastic model. *Journal of Rheology*, 22(3):259–283, 1978.

[18] H. Giesekus. A unified approach to a variety of constitutive models for polymer fluids based on the concept of configuration-dependent molecular mobility. *Rheologica Acta*, 21(4):366–375, Jul 1982.

[19] R. B. Bird, C. F. Curtiss, R. C. Armstrong, and O. Hassager. *Dynamics of Polymeric Liquids Vol. 1, Fluid Mechanics*. Wiley, New York, 1987.

[20] LL Ferrás, AM Afonso, JM Nóbrega, and FT Pinho. A numerical and theoretical study on viscoelastic fluid slip flows. *Physics of Fluids*, 29(5):053102, 2017.

[21] L. Campo-Deaño, R. P. A. Dullens, D. G. A. L. Aarts, F. T. Pinho, and M. S. N. Oliveira. Viscoelasticity of blood and viscoelastic blood analogues for use in polydymethylsiloxane in vitro models of the circulatory system. *Biomicrofluidics*, 7(034102), 2013.

[22] A. Ramiar, M. M. Larimi, and A. A. Ranjbar. Investigation of blood flow rheology using second-grade viscoelastic model (Phan-Thien-Tanner) within carotid artery. *Acta Bioeng. Biomech.*, 19(3), 2017.

[23] Nayyef Ahmed Talib and Özgür ErtunÇ. Application of giesekus model for capillary extrusion of rubber compound. *Journal of Chemical Engineering of Japan*, 52(2):185–193, 2019.

[24] Dahang Tang, Flávio H Marchesini, Dagmar R DâĂŹhooge, and Ludwig Cardon. Isothermal flow of neat polypropylene through a slit die and its die swell: Bridging experiments and 3d numerical simulations. *Journal of Non-Newtonian Fluid Mechanics*, 266:33–45, 2019.

[25] Zeeshan Khan, Rehan Ali Shah, Saeed Islam, Bilal Jan, Muhammad Imran, and Farisa Tahir. Steady flow and heat transfer analysis of phan-thein-tanner fluid in double-layer optical fiber coating analysis with slip conditions. *Scientific reports*, 6:34593, 2016.

[26] Alexandros Syrakos, Yannis Dimakopoulos, and John Tsamopoulos. Theoretical study of the flow in a fluid damper containing high viscosity silicone oil: Effects of shear-thinning and viscoelasticity. *Physics of Fluids*, 30(3):030708, 2018.

[27] LL Ferrás, AM Afonso, MA Alves, JM Nóbrega, and FT Pinho. Electro-osmotic and pressure-driven flow of viscoelastic fluids in microchannels: Analytical and semi-analytical solutions. *Physics of Fluids*, 28(9):093102, 2016.

[28] Harshad Sanjay Gaikwad, Prashant Baghel, Rajkumar Sarma, and Pranab Kumar Mondal. Transport of neutral solutes in a viscoelastic solvent through a porous microchannel. *Physics of Fluids*, 31(2):022006, 2019.

[29] J. Evans, I. L. Palhares Junior, and C. M. Oishi. Stresses of the oldroyd-b, ptt and giesekus fluids in a newtonian velocity field near the stick-slip singularity. *Physics of Fluids*, 29:1–33, 2017.

[30] J. Evans. Stick-slip and slip-stick singularities of the phan-thien-tanner fluid. *Journal Non-Newtonian Fluid Mechanics*, 199:12–19, 2013.

[31] J. Evans. Stick-slip singularity of the giesekus fluid. *Journal Non-Newtonian Fluid Mechanics*, 222:24–33, 2015.

[32] M. Renardy. How to integrate the upper convected maxwell (ucm) stresses near a singularity (and maybe elsewhere, too). *Journal of non-newtonian fluid mechanics*, 52(1):91–95, 1994.

[33] J. D. Evans and C. M. Oishi. Transient computations using the natural stress formulation for solving sharp corner flows. *Journal Non-Newtonian Fluid Mechanics*, 249:48–52, 2017.

[34] J. D. Evans, H. L. Franca, and C. M. Oishi. Application of the natural stress formulation for solving unsteady viscoelastic contraction flows. *Journal of computational physics*, 388(1):424–489, 2019.

[35] A. Fortin, A. Zine, and J.-F. Agassant. Computing viscoelastic fluid flow problems at low cost. *Journal of Non-Newtonian Fluid Mechanics*, 45(2):209 – 229, 1992.

[36] F. P. T. Baaijens. Application of low-order discontinuous galerkin methods to the analysis of viscoelastic flows. *Journal Non-Newtonian Fluid Mechanics*, 52:37–57, 1994.

[37] S.-C. Xue, R. I. Tanner, and N. Phan-Thien. Three-dimensional numerical simulations of viscoelastic flows–predictability and accuracy. *Comput. Methods Appl. Mech. Engrg.*, 180:305–331, 1999.

[38] G. Karapetsas and J. Tsamopoulos. On the stick-slip flow from slit and cylindrical dies of a phan-thien and tanner fluid model. i. steady state. *Physics of Fluids*, 21(12):123101, 2009.

[39] M. Renardy. The high weissenberg number limit of the ucm model and the euler equations. *Journal of non-newtonian fluid mechanics*, 69(2):293–301, 1997.

[40] P. Wapperom and M. Renardy. Numerical prediction of the boundary layers in the flow around a cylinder using a fixed velocity field. *Journal of non-newtonian fluid mechanics*, 125(1):35–48, 2005.

[41] M.I. Gerritsma and T.N. Phillips. On the characteristics and compatibility equations for the ucm model fluid. *ZAMM - Journal of Applied Mathematics and Mechanics / Zeitschrift fÃ¡ijr Angewandte Mathematik und Mechanik*, 88(7):523–539.

[42] M. I. Gerritsma and T. N. Phillips. On the use of characteristic variables in viscoelastic flow problems . *IMA Journal of Applied Mathematics*, 66(2):127–147, 04 2001.

[43] C. M. Oishi, F. P. Martins, M. F. Tome, J. A. Cuminato, and S. Mckee. Numerical solution of the extended pom-pom model for viscoelastic free surface flows. *Journal of Non-Newtonian Fluid Mechanics*, 166(3):165–179, 2011.

[44] A. J. Chorin and J. E. Marsden. *A mathematical introduction to fluid mechanics*, volume 3. Springer, 1990.

[45] D. L. Brown, R. Cortez, and M. L. Minion. Accurate projection methods for the incompressible navier–stokes equations. *Journal of computational physics*, 168(2):464–499, 2001.

[46] F. S. Sousa, C. M. Oishi, and G. C. Buscaglia. Spurious transients of projection methods in microflow simulations. *Computer Methods in Applied Mechanics and Engineering*, 285:659–693, 2015.

[47] G. Tryggvason, R. Scardovelli, and S. Zaleski. *Direct numerical simulations of gas–liquid multiphase flows*. Cambridge University Press, 2011.

[48] M. A. Alves, F. T. Pinho, and P. J. Oliveira. Benchmark solutions for the flow of oldroyd-b and ptt fluids in planar contractions. *Journal Non-Newtonian Fluid Mechanics*, 110:45–75, 2003.

[49] Y.-C. Ahn and M. E. Ryan. A finite difference analysis of the extrudate swell problem. *International journal for numerical methods in fluids*, 13(10):1289–1310, 1991.

[50] V. Ngamaramvaranggul and M. F. Webster. Computation of free surface flows with a taylor-galerkin/pressure-correction algorithm. *Int. J. Num. Meth. Fluids*, 33:993–1026, 2000.

[51] H.K. Moffatt. Viscous and resistive eddies near a sharp corner. *J. Fluid Mech.*, 18(1):1–18, 1964.

[52] M. Elliotis, G. Georgiou, and C. Xenophontos. Solution of the planar newtonian stick–slip problem with the singular function boundary integral method. *International journal for numerical methods in fluids*, 48(9):1001–1021, 2005.

Appendix A: Verification for Newtonian flow

We first verify the scheme for Newtonian flow, where the contribution of the non-Newtonian effects is neglected. Thus only step 1 of the algorithm is applied. The u velocity component along the free surface in Newtonian flow, is given by the expression [51]

$$u(x) = 2a_{\frac{1}{2}}x^{\frac{1}{2}} - 2a_{\frac{3}{2}}x^{\frac{3}{2}} + 2a_{\frac{5}{2}}x^{\frac{5}{2}} + O(x^{\frac{7}{2}}), \quad \text{as} \quad x \to 0, \tag{5.64}$$

near to singularity. This equation, together with the value in Table 4, may be used to calculate the coefficients $a_{\frac{1}{2}}$, $a_{\frac{3}{2}}$ and $a_{\frac{5}{2}}$ shown in Table 5. In this Section, we have considered the intermediate mesh M2, as defined in Table 1. Firstly, as can be seen in Table 5, our results compare well with those of the literature. In addition, we have plotted the horizontal velocity component u and the pressure p calculated along the stick-slip surface $y = 1$, as presented respectively in Figs. 26 and 27(a). Figure 27b) is presented as an additional comparison on the log – log scaling. According to these figures, we can confirm that our results are in good agreement with those numerical results presented by the literature.

Table 4: Set of values for x and u used to calculate the coefficients $a_{1/2}$, $a_{3/2}$ and $a_{5/2}$.

Values			
x	0.102512	0.499067	0.888449
u	0.4251695	0.8036053	0.9261778

Table 5: Coefficients of the expansion (5.64) near to the singularity for the Newtonian stick-slip flow.

Reference	$a_{1/2}$	$a_{3/2}$	$a_{5/2}$
Present work (M2)	0.69125	0.27154	0.05232
Karapetsas (M11, $h_{min} = 7.0e-06$) [38]	0.69157	0.27197	0.05247
Tanner and Huang (Analytical sol.) [6]	0.69099	–	–
Salamon et al. [7]	0.69160	0.27183	0.05232
Elliotis et al. [52]	0.69099	0.26450	0.03037

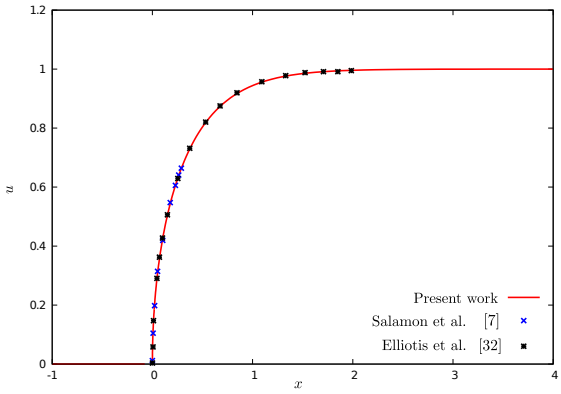

Figure 26: Comparison results for the velocity along the horizontal line $y = 1$.

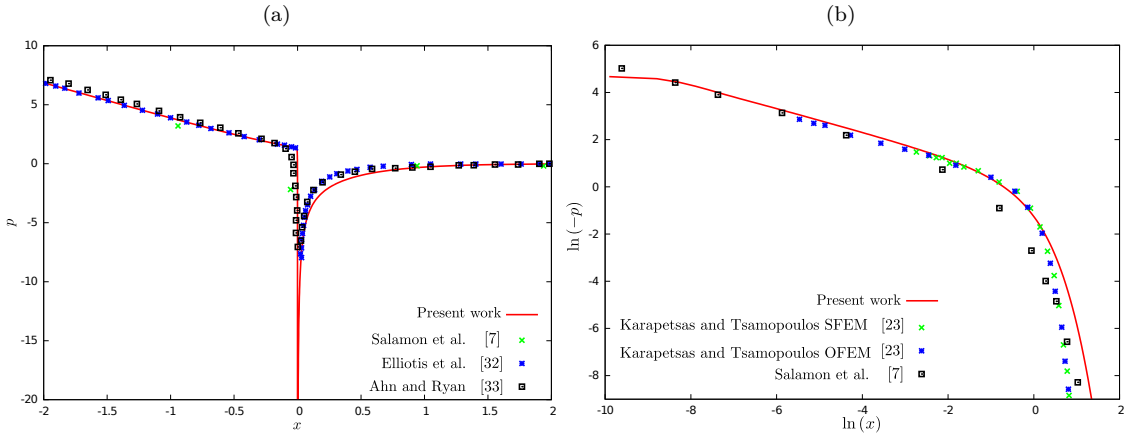

Figure 27: Comparison results for the pressure (a) and results for $\ln(-p)$ and $\ln(x)$ (b) along the horizontal line $y = 1$.

Appendix B: Effect of the truncation length for the stress singularity results

In this appendix, we have investigated the effect of the truncation length for capturing the numerical results in the vicinity of the stick-slip transition point. For this purpose, we have considered the PTT model on the M2 mesh, and considered three different dimensionless domain half-lengths, e.g., $L = 4$, $L = 8$ and $L = 16$ varying the Weissenberg number as 1, 5, 10 and 15. According to Figs. 28–29, we can confirm that the results for the velocity and pressure fields are very similar for the three truncation lengths. Moreover, it is relevant to highlight that the numerical results for extra-stress tensor and for

natural stress variables, presented respectively in Fig. 30 and Fig. 31, are also very similar for $L = 4$, $L = 8$ and $L = 16$ even for large Wi. Therefore, the dimensionless domain half-lengths adopted in our study did not influence the numerical results captured in the vicinity of the singularity.

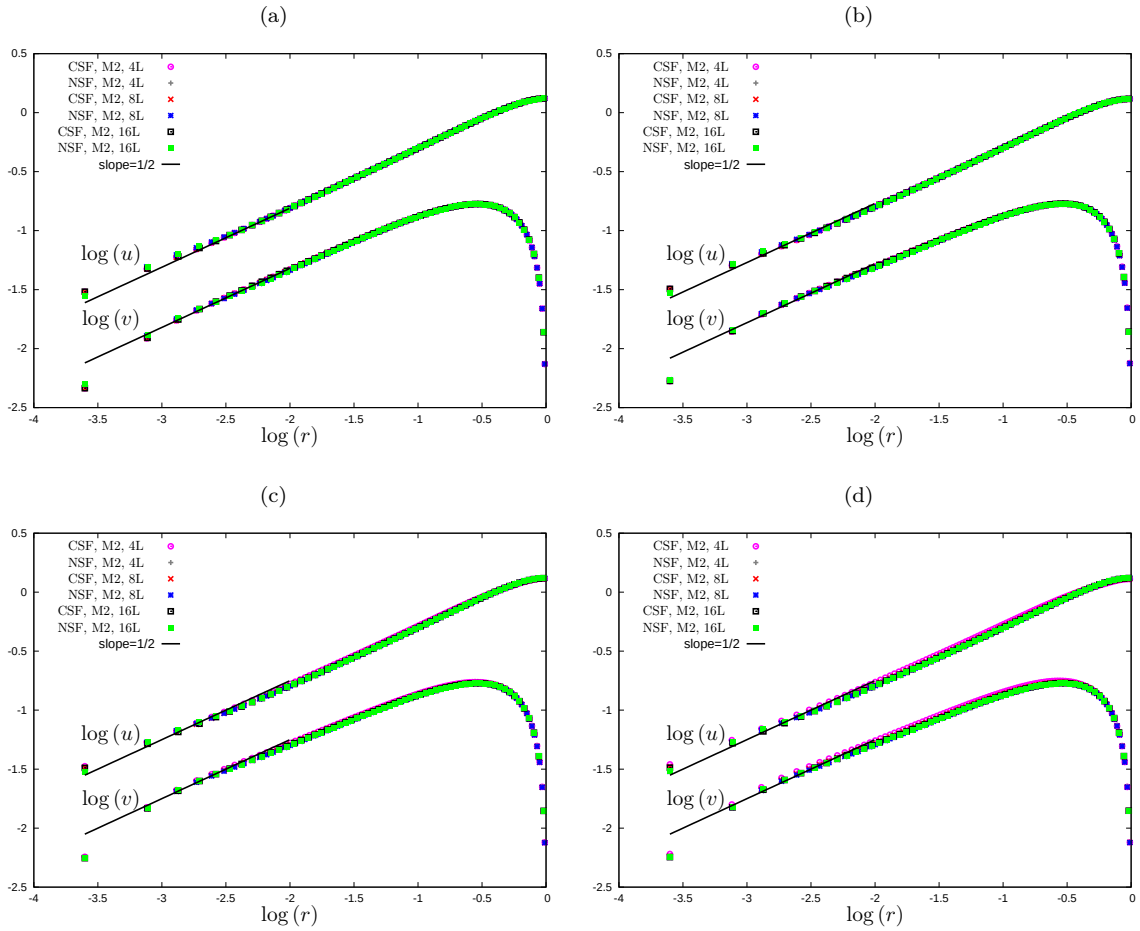

Figure 28: Asymptotic variation near the stick-slip transition point of u and v along the line $\theta = \pi/2$ for different values of Wi: (a) $Wi = 1$, (b) $Wi = 5$, (c) $Wi = 10$ and (d) $Wi = 15$.

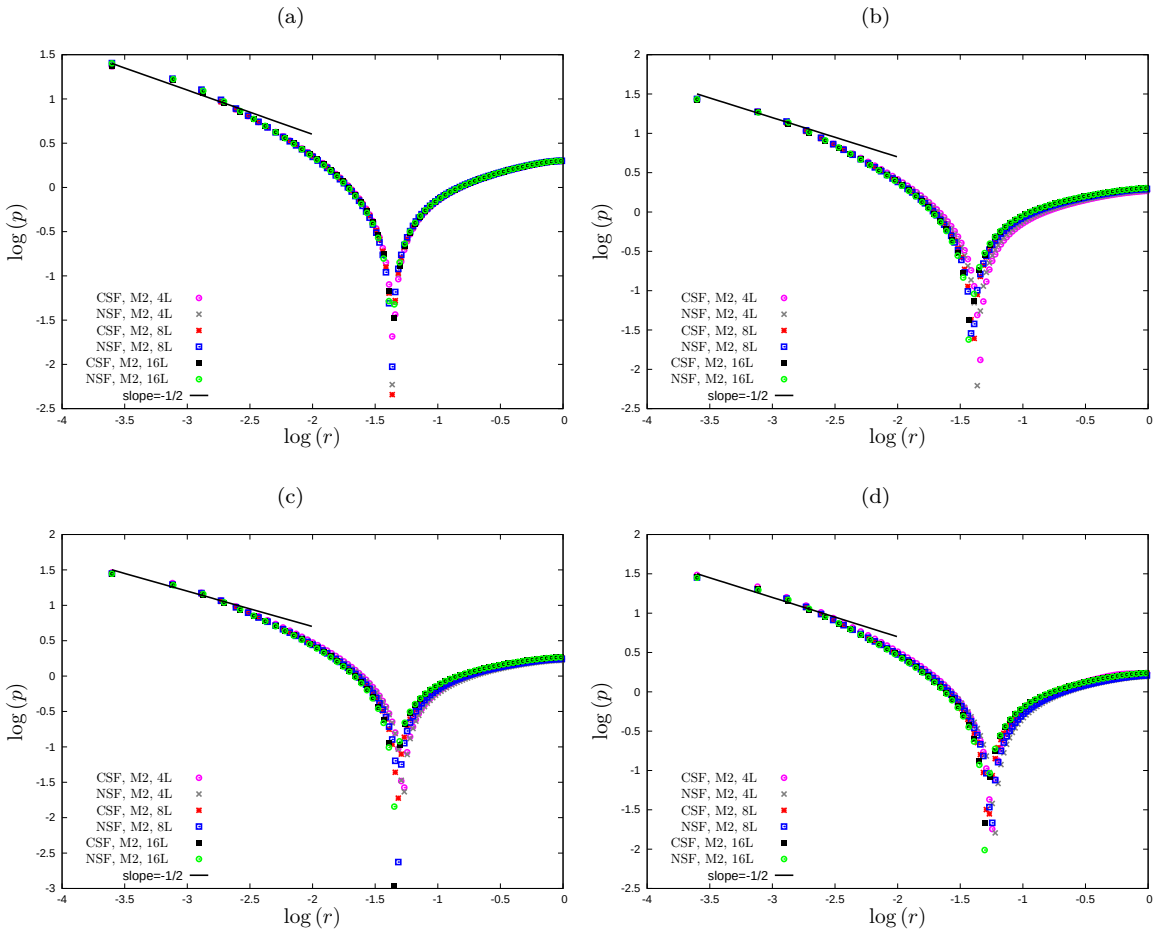

Figure 29: Asymptotic variation near the stick-slip transition point of p along the line $\theta = \pi/2$ for different values of Wi: (a) $Wi = 1$, (b) $Wi = 5$, (c) $Wi = 10$ and (d) $Wi = 15$.

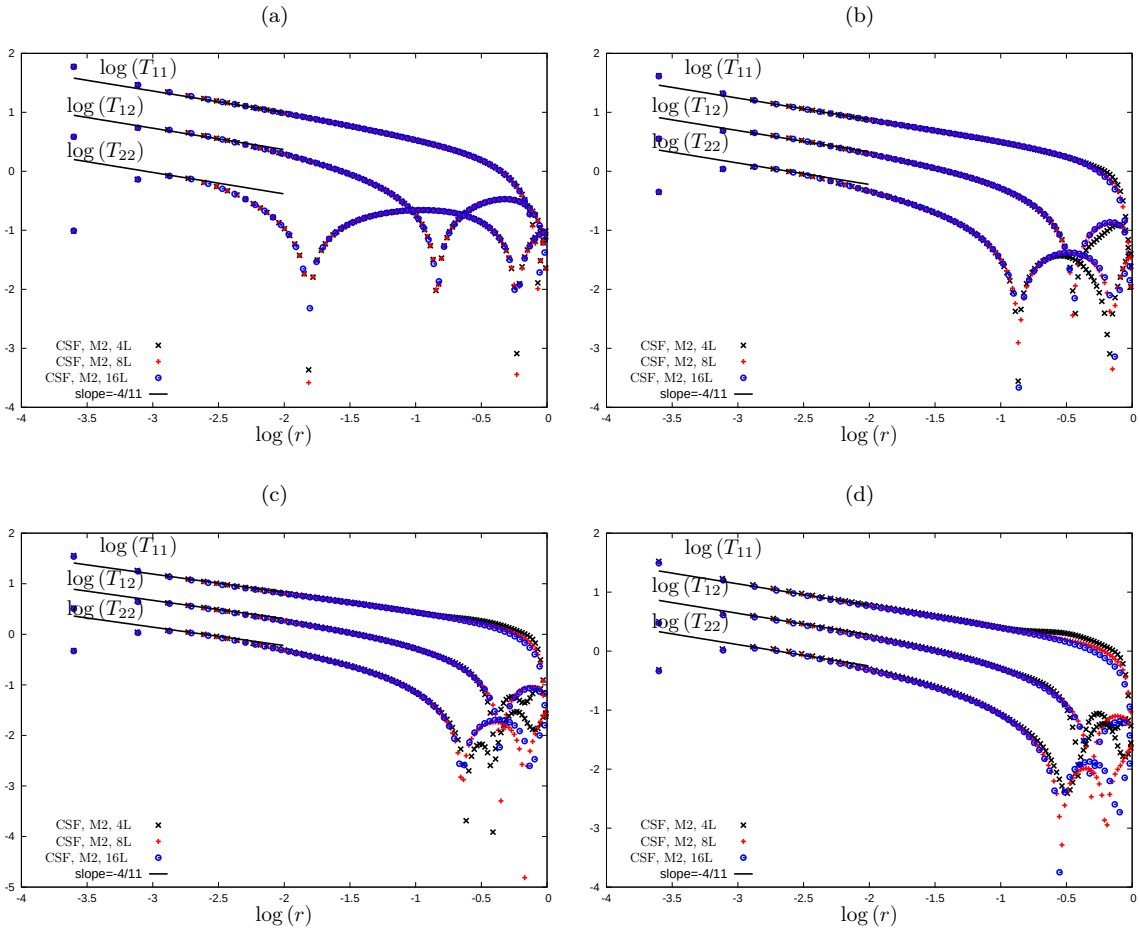

Figure 30: Asymptotic variation near the stick-slip transition point of T_{11}, T_{12}, T_{22}, λ, μ and ν along the line $\theta = \pi/2$ for different values of Wi: (a) $Wi = 1$, (b) $Wi = 5$, (c) $Wi = 10$ and (d) $Wi = 15$.

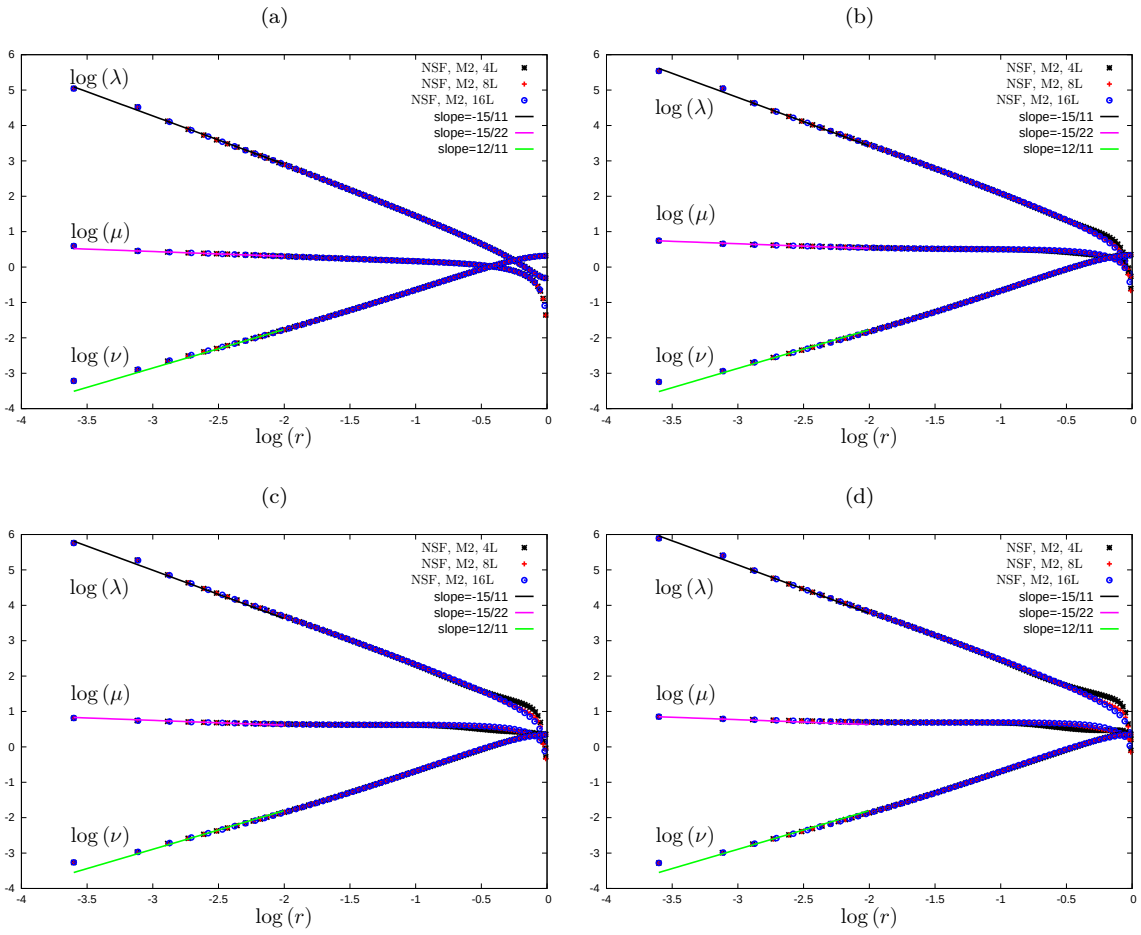

Figure 31: Asymptotic variation near the stick-slip transition point of λ, μ and ν along the line $\theta = \pi/2$ for different values of Wi: (a) $Wi = 1$, (b) $Wi = 5$, (c) $Wi = 10$ and (d) $Wi = 15$.